JOURNAL OF GEOPHYSICAL RESEARCH, VOL. 104, NO. A1, PAGES 395–411, JANUARY 1, 1999

Self-organization in the two-dimensional magnetohydrodynamic transverse Kelvin-Helmholtz instability

Akira Miura

Department of Earth and Planetary Physics, University of Tokyo, Tokyo

Abstract. For a two-dimensional transverse configuration in a compressible plasma a magnetohydrodynamic simulation of the Kelvin-Helmholtz (K-H) instability has been performed for a subfast shear flow. The simulation shows that after the linear growth and the subsequent nonlinear saturation of the fastest growing vortices these vortices are susceptible to vortex pairings, which occur because of the growth of subharmonics. The total kinetic energy remains almost constant in the evolution of the instability, but the enstrophy decreases rapidly owing to the selective dissipation by an artificial viscosity, which is added to prevent mesh oscillations. Therefore the nonlinear evolution of the two-dimensional transverse K-H instability, in particular, the successive pairings of vortices, are well described as a self-organization process resulting from the interplay of the nonlinearity and the dissipation. After the early stage of the instability development the kinetic energy and the squared vorticity cascade toward the long wavelength (inverse cascade) to form power law spectra in the wavenumber space. The inverse cascade in the wavenumber space corresponds, in the configuration space, to an emergence of a large isolated flow vortex and an associated eddy of inertia current out of trains of small-scale vortices and current eddies in the early stage. At the end of the simulation run the power law exponents in the wavenumber space of the kinetic energy, the squared vorticity, and the magnetic energy, which are all integrated across the initial flow direction, become -3.89, -2.08, and -4.58, respectively, in the intermediate wavenumber subrange.

1. Introduction

The sheared flow is a ubiquitous feature in space and astrophysical plasmas such as at the magnetopause, at the bow-shock, and in the solar wind. It is also commonly observed inside the magnetosphere as a consequence of several different magnetospheric dynamical processes. It is well known that such shear flows are susceptible to the Kelvin-Helmholtz (K-H) instability, which is also called the shear instability in hydrodynamics [e.g., *Dungey*, 1955; *Chandrasekhar*, 1961; *Southwood*, 1968; *Miura and Sato*, 1978a, b; *Walker*, 1981; *Miura and Pritchett*, 1982; *Pu and Kivelson*, 1983]. Observational evidence supporting the occurrence of the K-H instability at the terrestrial and planetary magnetopauses has been accumulated [e.g., *Lepping and Burlaga*, 1979; *Schardt et al.*, 1984; *Chen et al.*, 1993; *Seon et al.*, 1995; *Kivelson and Chen*, 1995]. The study of the nonlinear (finite-amplitude) evolution of the K-H instability is important in understanding the transport of momentum and energy [*Miura*, 1982, 1984] and an emergence of a large-scale order created by the instability. The pairing of vortices appearing in the evolution of the K-H instability is a well-known nonlinear effect. Several hydrodynamical experiments have shown that at the late stage of the K-H instability, two vortical structures combine to form a single, larger vortical structure [e.g., *Winant and Browand*, 1974; *Browand and Weidman*, 1976; *Ho and Huang*, 1982]. Such vortex pairing has also been reproduced by numerical experiments of the two-dimensional (2-D) hydrodynamics [e.g., *Lesieur et al.*, 1988; *Lele*, 1989] and 2-D magnetohydrodynamics (MHD) [*Wu*, 1986; *Belmont and Chanteur*, 1989; *Manuel and Samson*, 1993]. However, the pairing of vortices has not been studied quantitatively, and it is not even questioned why vortices merge in the nonlinear stage of the K-H instability.

The primary objective of the present study is to investigate the relevance of self-organization in the two-dimensional Navier-Stokes flow [e.g., *Rhines*, 1975; *Bretherton and Haidvogel*, 1976; *Kraichnan and Montgomery*, 1980; *McWilliams*, 1984; *Hasegawa*, 1985] to the nonlinear evolution of the K-H instability in the 2-D MHD transverse configuration by a 2-D MHD simulation and thus to throw a new light on the nonlinear evolution of the K-H instability, in particular, the successive pairings of vortices from the point of self-organization. Although the self-organization is a rather subjective concept [*Hasegawa*, 1985], the underlying concept of the self-organization, i.e., the emergence of macroscopic order out of disorder, is an important subject in a variety of disciplines from physics and chemistry to social sciences [see, e.g., *Wiener*, 1961; *Nicolis and Prigogine*, 1977; *Gell-Mann*, 1994; *Prigogine*, 1997]. The formation of life from primordial substances is an example of self-organization. *Wiener* [1961] discussed in detail a self-organizing process by which narrow, highly specific frequencies are formed in brain waves. The usefulness of the methods of the calculus of variations in studying the self-organized state is also pointed out by *Wiener* [1961]. In three-dimensional toroidal plasmas, *Taylor* [1974] proposed that the plasma will reach an equilibrium or a relaxed state, with minimum magnetic energy, by imposing a constraint of constant magnetic helicity. The process of relaxation to such a state is a self-organization

Paper number 98JA02530.
0148-0227/98/98JA-02530$09.00

process. The self-organization processes in MHD and plasma have also been studied quite intensively and extensively by computer simulations [e.g., *Matthaeus and Montgomery*, 1980; *Horiuchi and Sato*, 1986] (see also a recent review by *Sato and the Complexity Simulation Group* [1996]).

The self-organization in the 2-D, incompressible hydrodynamic turbulence is well known [e.g., *Kraichnan*, 1967; *Lilly*, 1969; *Rhines*, 1975; *Bretherton and Haidvogel*, 1976; *Kraichnan and Montgomery*, 1980; *Hasegawa*, 1985]. According to the self-organization in the 2-D incompressible turbulence, there are two inviscid global invariants, i.e., the total kinetic energy and the mean or total square vorticity (enstrophy), and when a small viscosity is added to the system, the total kinetic energy remains approximately constant, but the enstrophy decays rapidly by the selective dissipation [*Bretherton and Haidvogel*, 1976; *Kraichnan and Montgomery*, 1980] because of the viscosity. In the 2-D, incompressible hydrodynamics, the self-organization leads to the fact that the total kinetic energy cascades to the long wavelength (inverse energy cascade), or the vortex with the similarly signed vorticity must tend to group together. Since the total kinetic energy W remains relatively invariant but the enstrophy U cascades to short wavelengths and is dissipated by the selective dissipation, the appropriate variational principle is $\delta U - \lambda \delta W = 0$. This leads to the equation

$$\nabla \times \nabla \times \mathbf{v} = \lambda \mathbf{v} \tag{1}$$

which describes the minimum enstrophy state, which the 2-D turbulence is relaxed into [*Hasegawa*, 1985]. Here, $\mathbf{v}$ is the 2-D flow velocity vector, and λ is a constant.

The hydrodynamic and MHD K-H instability including vortex pairings has been studied quite intensively by computer simulations. *Metcalfe et al.* [1987] did a three-dimensional incompressible hydrodynamic simulation of the temporal evolution of the hyperbolic tangent velocity shear layer and found that the shear layer is susceptible to the 2-D K-H instability and that a vortex pairing occurs in the nonlinear stage when a properly tailored 2-D seed perturbation is given initially. They measured a spatially averaged Reynolds stress when the vortex pairing is inhibited and when it is allowed. *Lesieur et al.* [1988] did a 2-D incompressible hydrodynamic simulation of the temporal evolution of the hyperbolic tangent velocity shear layer. Starting from an initial white-noise perturbation, they found that four vortices appear initially in the simulation region and then they merge to form two vortices. They found that after the first vortex pairing the spatial longitudinal kinetic energy spectrum has a power law spectrum with a slope between k^{-4} and k^{-3}. *Lele* [1989] did 2-D compressible hydrodynamic simulations of both temporally growing and spatially growing free shear layers. He found that the pressure decreases inside the vortex and that vortex pairings occur in the nonlinear stage. He calculated energy spectra, but he did not follow the temporal evolution of the free shear layer until a single isolated vortex was formed by successive vortex pairings. *Wu* [1986] did 2-D compressible MHD simulations of the spatially growing K-H instability using a nonperiodic boundary condition for both transverse and parallel homogeneous configurations, where the initial magnetic field is transverse and parallel to the initial flow, respectively. He found in his simulation of the spatially growing K-H instability that the vortices excited by the K-H instability become larger in the downstream and the relaxation of the velocity shear by the instability is larger in the downstream. *Belmont and Chanteur* [1989] did a 2-D, compressible, resistive MHD simulation of the temporally growing K-H instability for a sheared magnetic configuration including a magnetic field component parallel to the flow and found successive pairings of the vortices. *Manuel and Samson* [1993] did a 2-D compressible MHD simulation of a spatially growing K-H instability using a nonperiodic boundary condition for an inhomogeneous configuration with a sheared magnetic field. They found vortex pairings in the downstream and also that the tangential stress by the instability becomes larger in the downstream. *Miura* [1997] clarified in detail the difference between the 2-D compressible hydrodynamic K-H instability and the 2-D compressible MHD transverse K-H instability and performed a 2-D compressible MHD simulation of the temporally growing K-H instability for a homogeneous transverse configuration, where the magnetic field is transverse to the flow. *Miura* [1997] investigated the basic relationship among vortex development including vortex pairing, rarefaction, and compression due to the fast magnetosonic wave, flow enhancement, eddy current, and momentum transport caused by the K-H instability in a compressible plasma or, more specifically, in a 2-D transverse configuration. In that study the length of the simulation system in the direction of the initial flow was equal to 4 times as long as the wavelength of the linearly fastest growing mode, and two successive vortex pairings were observed. In spite of these intensive studies of the 2-D hydrodynamic and MHD K-H instability, no previous simulations have ever calculated the temporal evolution of the enstrophy, and hence the self-organization process arising from the selective dissipation in the 2-D K-H instability was never clarified. Although *Miura* [1997] derived a conservation law of the enstrophy for a 2-D compressible MHD transverse configuration, he did not follow the temporal and spectral evolutions of two inviscid incompressible global invariants, i.e., the total kinetic energy and the enstrophy. Therefore the self-organization process in the 2-D MHD transverse K-H instability was not noticed in his study.

In order to study the relevance of the self-organization to the nonlinear evolution of the K-H instability a compressible MHD simulation of the K-H instability is performed in the present study for a subfast shear flow in the 2-D MHD transverse configuration, where the magnetic field is transverse to the flow, and both temporal and spectral evolutions of the two inviscid incompressible global invariants are studied. In the present study the length of the simulation system in the initial flow direction is equal to 8 times as long as the wavelength of the linearly fastest growing mode and thus twice as long as the simulation system used by *Miura* [1997]. In the present study it will be shown that basic physics clarified by *Miura* [1997] is also valid in the present longer simulation system with only a quantitative change. It is important to see that successive vortex pairings, i.e., the self-organization and the relaxation to the minimum enstrophy state, occur also for a larger simulation system for a computational reason. This demonstration of the successive vortex pairings for a longer simulation system is also important from a practical point of view because in a real magnetosphere it is anticipated that vortices created by the instability near the subsolar magnetopause undergo four or five vortex pairings during the passage of the vortices from the subsolar region to the tail of the magnetosphere.

The necessary condition for the self-organization in continuous media is the existence of several global invariants when there is no dissipation [*Hasegawa*, 1985]. However, when a small dissipation is added to the system, some invariants decay

more rapidly than other invariants because of the selective dissipation [*Montgomery et al.*, 1978; *Riyopoulos et al.*, 1982]. Therefore the existence of the ultimate dissipation is necessary in the self-organization, but the detail of the self-organization process does not seem to depend on the nature of the dissipation processes. In the present numerical simulation the dissipation needed for the self-organization is an artificial viscosity, which is added to prevent mesh oscillations. In the present study we do not ask what causes the real dissipation of the enstrophy in the collisionless space plasma, i.e., the nature of the collisionless viscosity, although it is due to microscopic processes (ion kinetics) in space plasmas. We note that this interrelationship of the MHD and the dissipation is analogous to other problems in space plasmas, such as collisionless shocks and reconnection, wherein the ultimate dissipation is necessary, but the final state attained in those problems is mainly determined by the global MHD consideration. We should also point out that although the ultimate dissipation of vorticity and energy is caused by the real viscosity, which makes the process irreversible, the transport of momentum and energy is governed by the development of turbulent large-scale eddies or vortices. For this reason a "viscosity," which is the measure of the transport of momentum and energy, is the anomalous viscosity [*Miura*, 1982, 1984] or the turbulent viscosity [*Landau and Lifshitz*, 1959], which is much larger than the real viscosity. It has been shown by the quasilinear analysis [*Miura and Sato*, 1978a, b; *Horton et al.*, 1987; *Rankin et al.*, 1997] that the anomalous viscosity is proportional to the square of the vortex amplitude. The discrepancy regarding the magnitude of the momentum transport and the anomalous viscosity caused by the K-H instability among previous studies by *Miura* [1984], *Wu* [1986], and *Manuel and Samson* [1993] will also be resolved in the present study by showing the increase of the momentum transport with the vortex pairing.

The outline of the present paper is as follows: A 2-D transverse configuration used in the present simulation is described and the conservation law of the enstrophy for the 2-D viscid compressible plasma (fluid) is derived in section 2. Simulation results for the 2-D MHD transverse configuration are shown in section 3. Discussion and summary are given in section 4.

2. Conservation Laws and 2-D Inviscid Incompressible Global Invariants

Figure 1 shows flow velocity and magnetic field in a 2-D MHD transverse configuration, which is used in the following 2-D MHD simulation. An initial uniform magnetic field $\mathbf{B_0}$ is transverse to the simulation plane (x-y plane). The background plasma flow is in the y direction, and the flow velocity v_y is inhomogeneous (sheared) in the x direction. In the 2-D transverse configuration the magnetic field $\mathbf{B}$ at any time remains transverse to the simulation plane (i.e., $\mathbf{B}$ has the only z component B_z), but $\mathbf{B}$ is not necessarily uniform because the magnetic field may be compressed or rarefied by the 2-D plasma motion in the x-y plane. The line bending term $(\mathbf{B} \cdot \nabla)\mathbf{B}$ in the $\mathbf{J} \times \mathbf{B}$ force in the equation of motion vanishes in the 2-D MHD transverse configuration. Therefore, in the equation of motion the effect of the magnetic field appears only in the total pressure $p_t = p + B^2/2\mu_0$, where p is the plasma pressure. In the 2-D transverse configuration it is shown that the density ρ and B_z remain proportional at any time [*Miura*, 1997]. The differences and the similarities between the 2-D fluid motion and the plasma motion in the 2-D MHD transverse configuration are discussed in detail by *Miura* [1997]. In short, when the plasma is compressible and the ratio of specific heats $\Gamma \neq 2$, B_z appears explicitly in the governing equations. Therefore, for $\Gamma \neq 2$, there is essentially a difference between the K-H instability in the 2-D MHD transverse configuration and the K-H instability in the 2-D hydrodynamic configuration. When the plasma is incompressible ($\nabla \cdot \mathbf{v} = 0$), the magnetic field and the density are not perturbed in the 2-D MHD transverse configuration, and the plasma behaves like an incompressible fluid. In the 2-D MHD transverse configuration used in the following simulation it is assumed that $\partial/\partial z = 0$, the initial density ρ_0 is uniform, and the ratio of specific heats Γ is equal to 5/3. Since ρ/B_z is initially uniform in the following 2-D MHD transverse configuration, ρ/B_z is an invariant of the plasma motion; that is, ρ and B_z remain proportional in the evolution of the K-H instability. In the 2-D inviscid and incompressible hydrodynamic flow the total kinetic energy and the enstrophy are two invariants of the fluid motion [e.g., *Onsager*, 1949; *Batchelor*, 1953; *Kraichnan*, 1967; *Montgomery*, 1989; *Biskamp*, 1993]. For the inviscid compressible plasma in the 2-D MHD transverse configuration the conservation law of the enstrophy was derived [*Miura*, 1997]. For the general viscid compressible plasma (or flow) in the 2-D MHD transverse configuration the conservation law of the enstrophy can be derived as follows: The equation of motion in the 2-D MHD transverse configuration can be written as

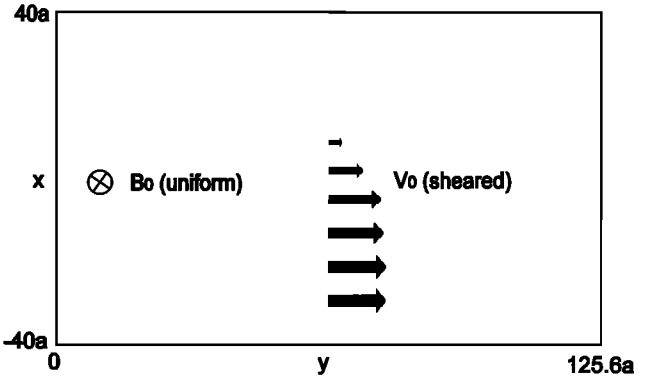

Figure 1. The sheared flow velocity (thick solid arrows) and the initial uniform magnetic field $\mathbf{B_0}$ in the two-dimensional (2-D) MHD transverse configuration.

$$\rho\left[\frac{\partial \mathbf{v}}{\partial t} + (\mathbf{v} \cdot \nabla)\mathbf{v}\right] = -\nabla p_t + \eta \nabla^2 \mathbf{v} \tag{2}$$

The last term in the right-hand side of (2) represents the viscous dissipation due to the artificial viscosity, which is added to prevent spurious mesh oscillations [*Richtmyer and Morton*, 1967; *Lapidus*, 1967; *Miura*, 1985]. By dividing (2) by ρ and by taking the curl of the resultant equation we obtain

$$\frac{\partial}{\partial t}(\nabla \times \mathbf{v}) + \nabla \times [(\mathbf{v} \cdot \nabla)\mathbf{v}] = \frac{\nabla \rho \times \nabla p_t}{\rho^2} + \nu \nabla^2 (\nabla \times \mathbf{v}) \tag{3}$$

where the vector product on the right-hand side, $\nabla \rho \times \nabla p_t/\rho^2$, is the baroclinic vector and $\nu = \eta/\rho$ is the kinematic viscosity. For simplicity, let us assume that ν is constant in space and in time. From (3) we obtain the following general conservation equation of the enstrophy (see *Hasegawa* [1985] for derivation

in the viscid incompressible case and *Miura* [1997] for derivation in the inviscid compressible case).

$$\frac{\partial}{\partial t}\int\int_C dxdy\ (\nabla\times\mathbf{v})^2 = -\int\int_C dxdy\ (\nabla\times\mathbf{v})^2(\nabla\cdot\mathbf{v}) + \int\int_C dxdy\ 2(\nabla\times\mathbf{v})\cdot\frac{(\nabla\rho\times\nabla p_i)}{\rho^2} - 2\nu\int\int_C dxdy\ (\nabla\times\boldsymbol{\Omega})^2 + 2\nu\int\int_A [\boldsymbol{\Omega}\times(\nabla\times\boldsymbol{\Omega})]\cdot d\mathbf{S} \quad (4)$$

where the left-hand side is proportional to the time derivative of the enstrophy (total square vorticity) and C represents a region in the x-y plane with $-x_b \le x \le x_b$ and $0 \le y \le L_y$ and A represents the surface surrounding the volume V, which consists of a region with $-x_b \le x \le x_b$, $0 \le y \le L_y$, and $0 \le z \le 1.0$. We assumed, as is also assumed in the following 2-D MHD simulation, that $\mathbf{v}$ is periodic in the y direction, i.e., $\mathbf{v}(x, y = 0) = \mathbf{v}(x, y = L_y)$, $v_x = 0$ at boundaries in the x direction at $x = \pm x_b$, and $\mathbf{v}$ is independent of z. We defined $\boldsymbol{\Omega} = \nabla\times\mathbf{v}$. Equation (4) gives the general conservation law of the enstrophy in C. In deriving the viscous terms in the right-hand side of (4) the following vector identity for the 2-D configuration was used:

$$\boldsymbol{\Omega}\cdot(\nabla^2\boldsymbol{\Omega}) = -\boldsymbol{\Omega}\cdot[\nabla\times(\nabla\times\boldsymbol{\Omega})] = -(\nabla\times\boldsymbol{\Omega})^2 + \nabla\cdot[\boldsymbol{\Omega}\times(\nabla\times\boldsymbol{\Omega})] \quad (5)$$

In the present 2-D MHD transverse configuration, where the initial quantities ρ_0 and $\mathbf{B_0}$ are uniform, ρ and B_z remain proportional. Therefore the baroclinic vector $\nabla\rho\times\nabla p_i/\rho^2$ is equal to $\nabla\rho\times\nabla p/\rho^2$, which is the same as the baroclinic vector in the hydrodynamic case. If the plasma (fluid) is uniform initially and incompressible ($\nabla\cdot\mathbf{v} = 0$), the density ρ is not perturbed and $\nabla\rho = 0$. Therefore we recover from (4) that in the 2-D uniform, inviscid, incompressible plasma (fluid) the enstrophy is an invariant of the plasma (fluid) motion. In a more general case, where the plasma (fluid) is viscous or the plasma (fluid) is compressible or the baroclinic vector is nonzero, the enstrophy is not an invariant of the 2-D plasma (fluid) motion.

In the inviscid 2-D MHD transverse configuration ($\mathbf{B}\perp\mathbf{v}$), taking the volume integral of the energy conservation equation and using the boundary condition in the present simulation lead to [*Miura*, 1997]

$$\frac{\partial}{\partial t}\int\int_C dxdy\left(\frac{1}{2}\rho v^2 + \frac{B^2}{2\mu_0} + \frac{p}{\Gamma-1}\right) = 0 \quad (6)$$

This is the conservation law of the total energy in the C region. In the uniform, incompressible case ($\Gamma\to\infty$), B_z and ρ are not perturbed and $\rho = \rho_0$. Therefore

$$\frac{\partial}{\partial t}\int\int_C dxdy\ v^2 = 0 \quad (7)$$

This means that the total kinetic energy is an invariant in the 2-D uniform, inviscid, incompressible case. Therefore, in the inviscid, incompressible, 2-D MHD transverse configuration or in the inviscid, incompressible, 2-D fluid, there are two global invariants of the plasma (fluid) motion, the enstrophy and the total kinetic energy.

3. Simulation Results

3.1. Initial Configuration and Initial Perturbation

A 2-D MHD simulation is performed in the x-y plane perpendicular to the magnetic field. The initial flow velocity v_{0y} has a hyperbolic tangent shear profile

$$v_{0y}(x) = (V_0/2)[1 - \tanh(x/a)] \quad (8)$$

and the other initial quantities (B_0, p_0, and ρ_0) are uniform. Therefore the initial velocity shear layer is characterized by the finite thickness of the velocity shear layer (2a). We impose a boundary condition such that there is no mass flow ($v_x = 0$) across the boundaries at $x = \pm x_b = \pm 40a$ and all quantities are periodic in the y direction [*Miura*, 1984]. Since the real frequency of the K-H instability is due to the Doppler shift due to the mean bulk flow the dispersion relation gives $\omega_r = k_y V_0/2$, where ω_r is the real part of the angular frequency. The appropriate Mach number for the background flow is the fast magnetosonic Mach number defined by $M_f = V_0/\sqrt{C_s^2 + V_A^2}$, where $V_A = B_0/(\mu_0\rho_0)^{1/2}$ and $C_S = (\Gamma p_0/\rho_0)^{1/2}$. Notice that an important Mach number, which characterizes the intrinsic compressibility of the flow, is the convective Mach number $M_{fc} = M_f/2$, which is the Mach number in a frame of reference comoving with the phase velocity of the unstable K-H wave [*Papamoshou and Roshko*, 1988].

In the present simulation run we adopt the sound Mach number $M_S = V_0/C_S = 1.0$ and the Alfvén Mach number $M_A = V_0/V_A = 1.0$. The fast mode Mach number M_f is $M_f = 0.71$, and the convective fast magnetosonic Mach number is $M_{fc} = 0.35$. We use a time T normalized by $2a/V_0$. For this configuration the linearly fastest growing mode occurs at $2k_y a \sim 0.8$ with its growth rate equal to $0.17V_0/2a$ [*Miura and Pritchett*, 1982]. Therefore the wavelength of the linearly fastest growing mode (FGM) λ_{FGM} is equal to $15.7a$. The length L_y of the simulation system in the y direction is chosen equal to $8\lambda_{FGM} = 125.6a$. Since the present simulation is an MHD simulation it is necessary to give explicitly an initial seed perturbation at $T = 0$. In the present simulation a linear superposition of the approximate linear eigenfunction of the fastest growing mode in the incompressible case [*Miura and Sato*, 1978a, b] and its subharmonic modes is added to the background flow at $T = 0$ as an initial seed perturbation [see also *Miura*, 1997]. The peak amplitude of the initial flow velocity perturbation is $0.005V_0$. The explicit form of the seed perturbation is as follows:

$$v_x(x, y) = \sum_{n=1}^{4} 2k_n[-\phi_r(x)\sin(k_n y) - \phi_i(x)\cos(k_n y)] \quad (9)$$

$$v_y(x, y) = -\sum_{n=1}^{4} 2\left[\frac{d\phi_r(x)}{dx}\cos(k_n y) - \frac{d\phi_i(x)}{dx}\sin(k_n y)\right] \quad (10)$$

where

$$k_n = k_{FGM}/2^{n-1} = (0.8/2a)/2^{n-1} \qquad n = 1, 2, 3, 4 \tag{11}$$

$$\phi_r(x) = \Psi_0 \exp\left(-\frac{x^2}{a^2}\right) \cos\left[\frac{\pi}{2} \sin\left(\frac{\pi x}{2a}\right)\right] \tag{12}$$

$$\phi_i(x) = \Psi_0 \exp\left(-\frac{x^2}{a^2}\right) \sin\left[\frac{\pi}{2}\sigma \sin\left(\frac{\pi x}{2a}\right)\right] \tag{13}$$

Ψ_0 is the arbitrary constant to determine the amplitude of the initial perturbation, and σ determines the inclination of the vortex with respect to the mean flow, which determines whether the vortex is growing or decaying [*Miura and Sato*, 1978a]. That is, $\sigma = -1$ for the growing vortex, and $\sigma = 1$ for the decaying vortex. The wavenumber k_{FGM} is the wavenumber of the linearly fastest growing mode. The conservation equations of the ideal MHD were solved by using the two-step Lax-Wendroff scheme and the number of grids is equal to 400×400.

3.2. Temporal Evolution of the 2-D Inviscid Incompressible Invariants

Figure 2 shows temporal evolutions of the total energy (dotted curve), total internal energy (dashed curve), total magnetic energy (dot-dashed curve), and the total kinetic energy (solid curve) integrated in the whole simulation region. Each total energy is normalized by $0.0628a^2p_0$. It is obvious from Figure 2 that there is almost no energy exchange between the total magnetic energy and the total kinetic energy. The total kinetic energy remains almost constant during the simulation run in the present 2-D transverse configuration.

Figure 3 shows temporal evolutions of the total square vorticity integrated in the whole simulation region (solid curve), the first term in the right-hand side of (4) due to the compressibility (dotted curve), and the second term in the right-hand side of (4) (dashed curve), which includes the baroclinic vector. It is obvious in Figure 3 that the enstrophy (total square vorticity) decreases rapidly with time with a small oscillating component. Comparison of the evolution of the total square vorticity and the compressible term, which shows a small net decrease, in Figure 3, indicates that the oscillating component in the enstrophy evolution is due to the compressibility, which is expressed by the first term in the right-hand side of (4). It is also seen in Figure 3 that the baroclinic term, which is the second term in the right-hand side of (4), is negligible compared with other terms in (4). Therefore we conclude that the large decrease in the enstrophy shown in Figure 3 must be due to the viscous dissipation, which is expressed by the last two terms in the right-hand side of (4). Notice that although the present simulation is done for the ideal MHD without any explicit physical viscosity, a small artificial viscosity is added to prevent spurious mesh oscillations. Therefore the enstrophy, which is the invariant in the 2-D, inviscid, and incompressible case, decreases with time because of the selective dissipation by the artificial viscosity. The constancy of the total kinetic energy shown in Figure 2 and the selective decay of the enstrophy shown in Figure 3 indicate that the evolution of the K-H instability in the present 2-D MHD transverse configuration is a self-organization process.

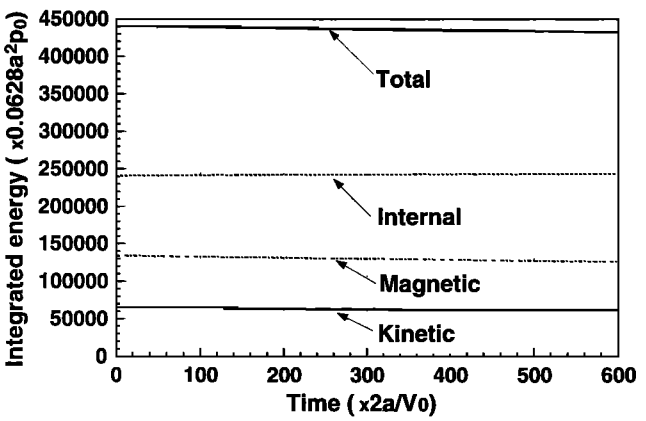

Figure 2. Temporal evolution of the total energy in the simulation region (dotted curve), total internal energy (dashed curve), total magnetic energy (dot-dashed curve), and the total kinetic energy (solid curve) integrated in the whole simulation region.

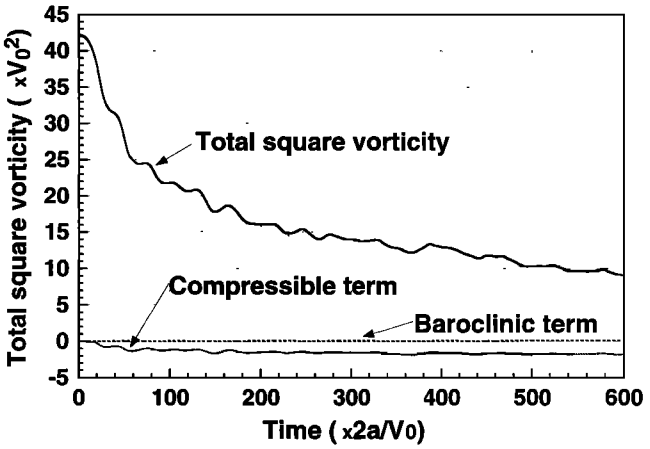

Figure 3. Temporal evolution of the total square vorticity (enstrophy) integrated in the whole simulation region (solid curve), the first term in the right-hand side of (4) due to the compressibility (dotted curve), and the second term (baroclinic term) in the right-hand side of (4).

3.3. Evolution in the Wavenumber Space

Let us define the kinetic energy spectrum integrated along x. According to the Parseval relation in the Fourier analysis we obtain

$$\frac{1}{2}a_0(x)^2 + \sum_{n=1}^{\infty}[a_n(x)^2 + b_n(x)^2] = \frac{2}{L_y}\int_0^{L_y}[f(x, y)]^2\,dy \tag{14}$$

where any function $f(x, y)$ defined in the x-y plane is expressed by the Fourier series as

$$f(x, y) = \frac{1}{2}a_0(x) + \sum_{n=1}^{\infty}\left[a_n(x)\cos\left(\frac{2\pi ny}{L_y}\right) + b_n(x)\sin\left(\frac{2\pi ny}{L_y}\right)\right] \tag{15}$$

$$a_n(x) = \frac{2}{L_y}\int_0^{L_y} f(x, y)\cos\left(\frac{2\pi ny}{L_y}\right)dy \tag{16}$$

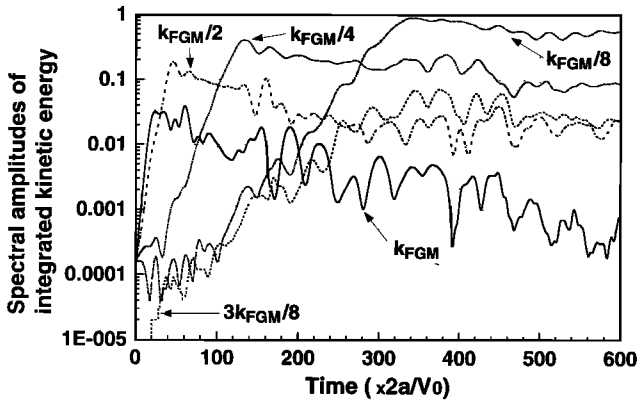

Figure 4. Temporal evolution of the amplitudes of the fastest growing mode with $k = k_{FGM}$ (solid curve), the first subharmonic with $k = k_{FGM}/2$ (dot-dashed curve), the second subharmonic with $k = k_{FGM}/4$ (dotted curve), the third subharmonic with $k = k_{FGM}/8$ (double dot-dashed curve), and the Fourier mode with $k = 3k_{FGM}/8$ (dashed curve) of the kinetic energy integrated along x. All amplitudes are normalized by $2ap_0$.

$$b_n(x) = \frac{2}{L_y}\int_0^{L_y} f(x, y)\,\sin\left(\frac{2\pi n y}{L_y}\right) dy \tag{17}$$

By integrating (14) from $x = -x_b$ to $x = x_b$ we obtain

$$\int_{-x_b}^{x_b} dx \left\{\frac{1}{2}a_0(x)^2 + \sum_{n=1}^{\infty}[a_n(x)^2 + b_n(x)^2]\right\}$$

$$= \int_{-x_b}^{x_b} dx \frac{2}{L_y}\int_0^{L_y}[f(x, y)]^2\, dy$$

If we define

$$S_n^2 = \int_{-x_b}^{x_b} dx\,[a_n(x)^2 + b_n(x)^2] \tag{19}$$

S_n^2 is equal to the contribution of the nth Fourier harmonic to $F(y)$, where

$$F(y) = \int_{-x_b}^{x_b} dx\,[f(x, y)]^2 \tag{20}$$

Therefore, if we take

$$f(x, y) = \sqrt{\frac{\rho(x, y)}{2}(v_x^2 + v_y^2 + v_z^2)} \tag{21}$$

then according to (18) and (19), (19) represents the contribution of the nth harmonic to the total kinetic energy. Similarly, if we take

$$f(x, y) = (\nabla \times \mathbf{v}) \cdot \hat{\mathbf{z}} \tag{22}$$

(19) represents the contribution of the nth harmonic to the total square vorticity (enstrophy).

Figure 4 shows temporal evolutions of Fourier amplitudes S_n^2 of the kinetic energy integrated along x. The five modes have the wavenumbers k equal to $k_{FGM}/8$ (double dot-dashed curve), $k_{FGM}/4$ (dotted curve), $3k_{FGM}/8$ (dashed curve), $k_{FGM}/2$ (dot-dashed curve), and k_{FGM} (solid curve), where k_{FGM} is the wavenumber of the linearly fastest growing mode. Each mode amplitude is normalized by $2ap_0$. At $T = 0$, four modes with $k = k_{FGM}$ (fastest growing mode), $k_{FGM}/2$ (first subharmonic), $k_{FGM}/4$ (second subharmonic), and $k_{FGM}/8$ (third subharmonic) have the same amplitudes (see (9)–(13)). The fastest growing and first subharmonic modes grow almost linearly in their linear phases. The growth rates of those modes were calculated from their linear slopes in the initial growth phases. The calculated growth rates are $0.161V_0/2a$ and $0.108V_0/2a$ for the fastest growing mode and the first subharmonic mode, respectively. The growth rates obtained by linear analysis for these two modes are $0.17V_0/2a$ and $0.12V_0/2a$, respectively [*Miura and Pritchett*, 1982]. Therefore there is good agreement between the predicted linear growth rates and the linear growth rates obtained from the simulation run. Although the fastest growing mode (solid curve) has the largest growth rate, the third subharmonic reaches the largest amplitude during the simulation run.

Figure 5 shows the spectral amplitudes S_n^2 of the integrated kinetic energy versus the wavenumber in the spectral space at six different times. The amplitude is normalized by $2ap_0$. In Figure 5, k_{min} is the wavenumber of the third subharmonic, which is equal to $k_{FGM}/8$. At $T = 0$ a velocity perturbation, as defined by (9)–(13), with small amplitude was added to the background flow velocity. As is shown by (9) and (10), the velocity perturbation is a linear combination of the fastest growing mode and the three subharmonics. The amplitudes of those modes were taken to be equal at $T = 0$. Therefore it is seen at $T = 0$ that there are four discrete peaks of the spectral amplitudes at $k = k_{min}$, $2k_{min}$, $4k_{min}$, and $8k_{min}$ with the same amplitudes. It is also seen at $T = 0$ that there are irregular noise components at large k values ($k/k_{min} > 90$). These noise components appeared possibly because of the round off errors or the inaccurate representation of the trigonometric functions in calculations of (16) and (17) by the finite difference method. Since these noise components are much smaller in amplitude than the initial seed perturbations at $k = k_{min}$, $2k_{min}$, $4k_{min}$, and $8k_{min}$ by more than 4 or 5 orders of magnitude, these irregular noise components do not play any important role in the present simulation. Since these noise components appeared at $T = 0$ before the numerical integration they are not due to the inaccuracy of the two-step Lax-Wendroff scheme. At $T = 20$, when the fastest growing mode has an initial peak in Figure 4, the spectral component with $k = 8k_{min}$ peaks, but later the spectral peak shifts to the smaller wavenumber, and finally, at $T = 600$ the spectral component at $k = k_{min}$ peaks owing to the inverse cascade of the integrated kinetic energy. Figure 5 shows that there are multiple discrete spectral peaks at the higher harmonics of the fastest growing modes and the subharmonics until $T = 90$. However, the spectral distribution becomes more continuous after $T = 90$ owing to the nonlinear coupling among higher harmonics. At $T = 600$ the spectral distribution becomes almost continuous and is well represented by a power law distribution. It can be seen in this figure that in the k space the kinetic energy cascades toward the short wavelength (direct cascade) in the early stage of the instability development, but the kinetic energy cascades toward the long wavelength (inverse cascade) after the early stage of the instability development.

Figure 6 shows the spectral amplitudes S_n^2 of the enstrophy (total square vorticity) versus the wavenumber in the spectral

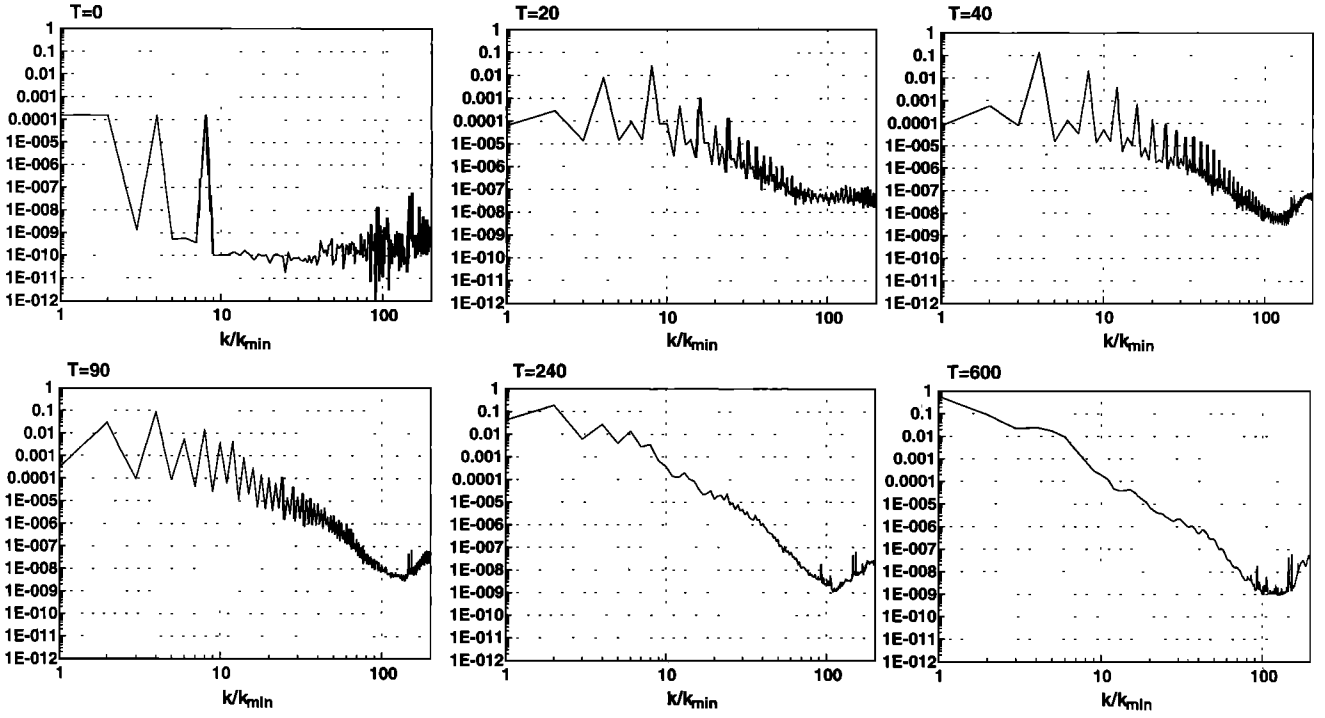

Figure 5. The spectral amplitudes S_n^2 of the kinetic energy integrated along x versus the wavenumber in the wavenumber space at six different times. The wavenumber is normalized by $k_{\min} = k_{\mathrm{FGM}}/8$.

space at six different times. The spectral amplitude (19) is calculated by using (22). The amplitude is normalized by $(V_0/2a)^2$. The spectral amplitude is shown in the same format as Figure 5. At $T = 0$, there are four discrete peaks at $k = k_{\min}$, $2k_{\min}$, $4k_{\min}$, and $8k_{\min}$. It is also seen at $T = 0$ that there are noise components at large k values ($k/k_{\min} > 90$) as was seen in Figure 5. These noise components at the initial Fourier spectra of the enstrophy are again possibly due to the round off

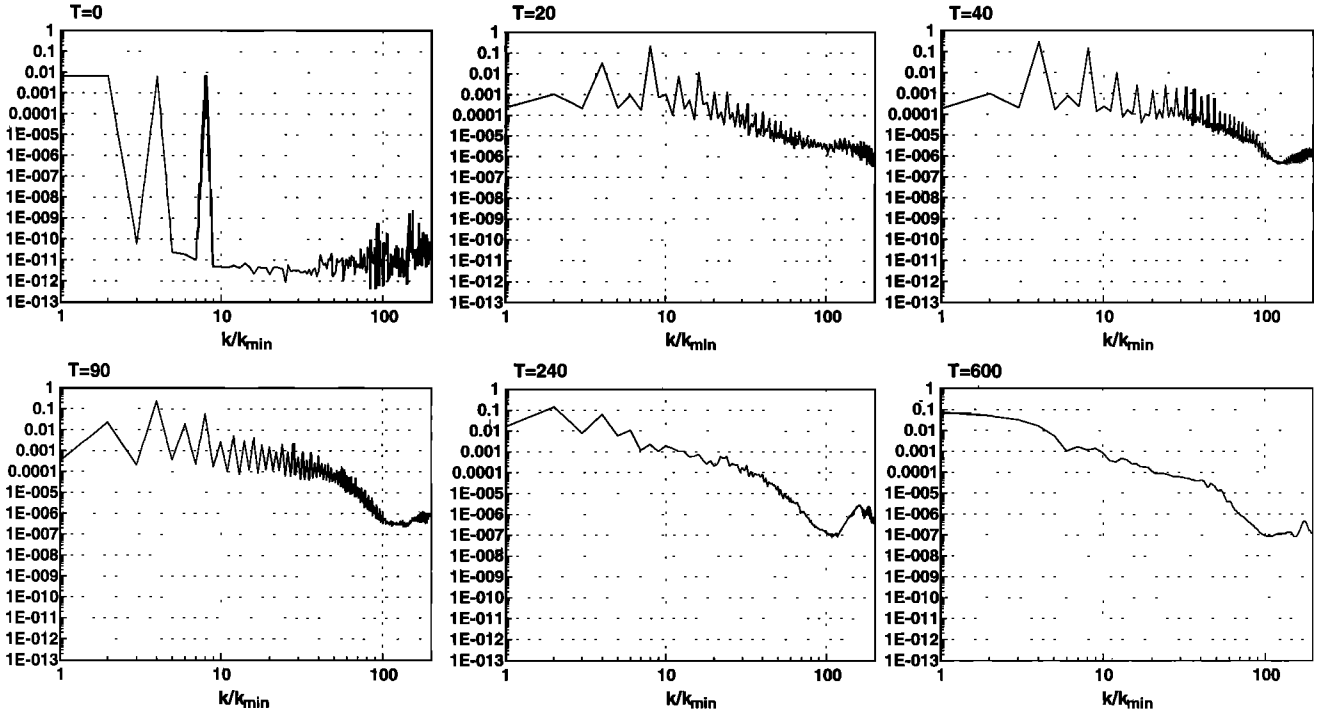

Figure 6. The spectral amplitudes S_n^2 of the enstrophy (total square vorticity) versus the wavenumber in the spectral space at six different times. The wavenumber is normalized by $k_{\min} = k_{\mathrm{FGM}}/8$.

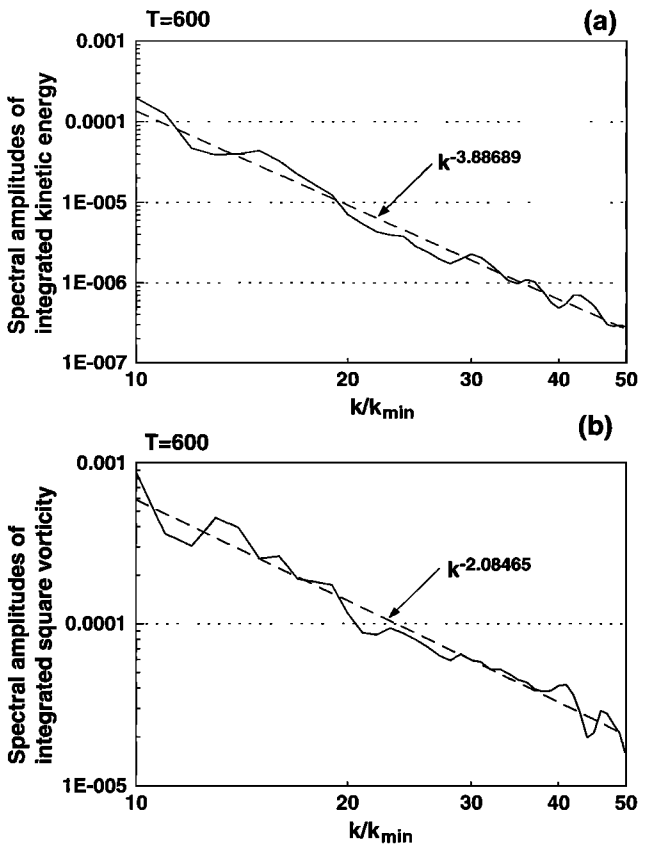

Figure 7. (a) The spectral distribution of the kinetic energy integrated along x shown in Figure 5 at medium range of the wavenumber from k/k_{min} = 10 to 50 at T = 600. The dashed line is a regression line, which fits most to the spectral distribution. The regression line has a power law exponent of −3.88689. (b) The spectral distribution of the enstrophy shown in Figure 6 at medium range of the wavenumber from k/k_{min} = 10 to 50 at T = 600. The dashed line is a regression line, which fits most to the spectral distribution. The regression line has a power law exponent −2.08465.

errors or the inaccurate representation of the trigonometric functions in calculations of (16) and (17) by the finite difference method. Since these noise components are smaller than the initial seed perturbation at $k = k_{min}$, $2k_{min}$, $4k_{min}$, and $8k_{min}$ by more than 7 or 8 orders of magnitude they do not play any important role in the present calculation. They are again not due to the inaccuracy of the two-step Lax-Wendroff scheme. At T = 20 the spectral component at $k = 8k_{min}$ peaks. There are multiple discrete spectral peaks at the higher harmonics of the fastest growing mode and the subharmonics until T = 90. However, the spectral distribution becomes more continuous owing to the nonlinear coupling among higher harmonics after T = 90. At T = 600 the spectral distribution becomes almost continuous and is well represented by a power law. In contrast to the spectral distribution at T = 600 of the integrated kinetic energy shown in Figure 5, the spectral peak at $k = k_{min}$ of the enstrophy is not sharp. It can be seen in Figure 6 that in the k space the enstrophy cascades toward the short wavelength (direct cascade) in the early stage of the instability development, but the enstrophy cascades toward the long wavelength (inverse cascade) after the early stage of the instability development.

Since the continuous spectra of both total kinetic energy and the enstrophy at T = 600 show power law distributions it is possible to obtain the power law exponents of those spectra at T = 600. The solid line in Figure 7a shows the spectral distribution of the total kinetic energy shown in Figure 5 at medium subrange of the wavenumber from k/k_{min} = 10 to 50 at T = 600. The dashed line is a regression line, which fits most to the spectral distribution of the total kinetic energy. This line has a power law exponent −3.88689. The solid line in Figure 7b shows the spectral distribution of the enstrophy shown in Figure 6 at medium subrange of the wavenumber from k/k_{min} = 10 to 50 at T = 600. The dashed line is a regression line, which fits most to the spectral distribution of the enstrophy. This line has a power law exponent −2.08465. Since the enstrophy is an integral of the square of the curl of v the observed fact that the power law exponent of the enstrophy is nearly equal to the power law exponent of the total kinetic energy plus 2 is reasonable.

Since S_n^2 represents the contribution or weight of the nth Fourier component to the total kinetic energy or the enstrophy the average wavenumber of the total kinetic energy or the enstrophy is calculated by the following formulae

$$\langle k \rangle = \frac{\sum_{n=1}^{\infty} k_n S_n^2}{\sum_{n=1}^{\infty} S_n^2} \tag{23}$$

Figure 8 shows the time evolutions of the average wavenumbers obtained by (23). The average wavenumbers are normalized by k_{FGM}. The solid line is the average wavenumber weighted by the integrated kinetic energy spectrum. Initially, the average wavenumber increases rapidly (direct cascade) and reaches 1.0 when the fastest growing mode is peaked, but thereafter, the average wavenumber decreases with time (inverse cascade). This gives evidence of the inverse energy cascade in the nonlinear stage. The dashed line is the average wavenumber weighted by the integrated square vorticity. The average wavenumber increases rapidly in the linear phase (direct cascade), but thereafter, the average wavenumber de-

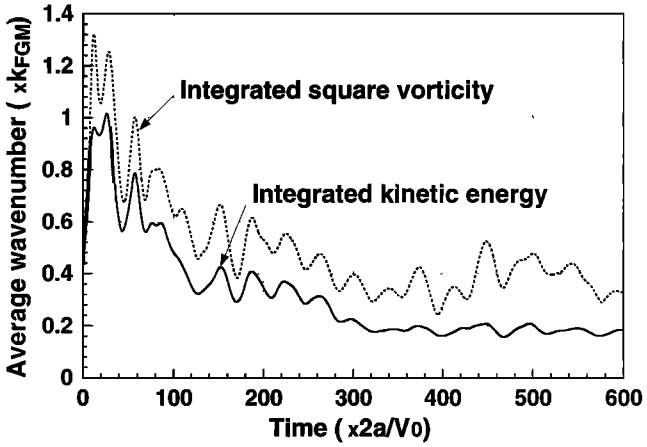

Figure 8. The time evolution of the wavenumbers averaged by using the spectral weight of integrated kinetic energy (solid curve) and the integrated square vorticity (dashed curve). The average wavenumbers are normalized by k_{FGM}.

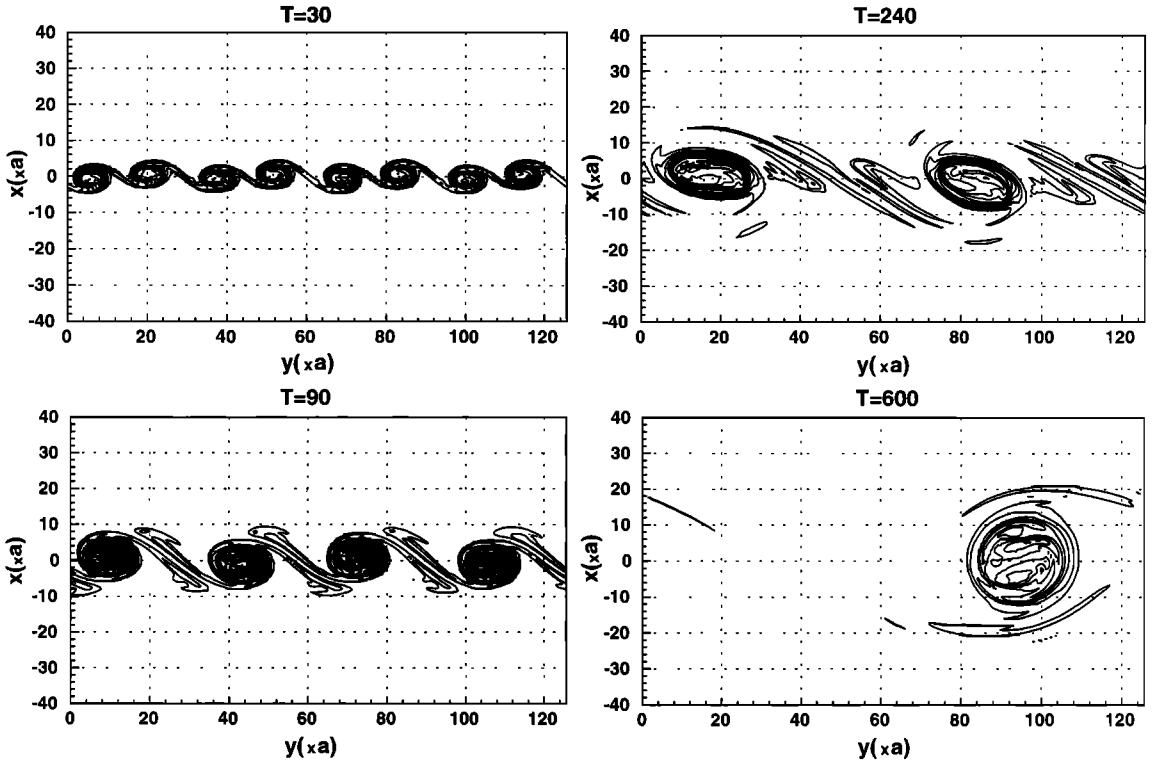

Figure 9. Contour lines of the z component of the vorticity at four different times from $T = 30$ to $T = 600$. The contour lines are plotted for negative vorticity (counterclockwise rotation).

creases with time (inverse cascade). Notice that the direct enstrophy cascade in the early stage is much stronger than that of the kinetic energy owing to the selective decay.

3.4. Evolution in the Configuration Space

Figure 9 shows contour lines of the z component of the vorticity Ω_z at four different times from $T = 30$ to $T = 600$. In the 2-D transverse configuration, Ω_z is calculated from the frozen-in law as

$$\Omega_z = \hat{\mathbf{z}} \cdot (\nabla \times \mathbf{v}) = -\frac{1}{B} \nabla \cdot \mathbf{E} + \frac{\mu_0}{B} (\mathbf{J} \cdot \mathbf{v}_\perp). \quad (24)$$

where $\mathbf{E}$ is the electric field satisfying the frozen-in law and $\mathbf{J}$ is the electric current density. Therefore, in the 2-D incompressible plasma, where the density ρ and $\mathbf{B}$ are not perturbed, the perturbation is electrostatic, $\mathbf{J}$ is zero, and the vorticity is proportional to the space charge density. In Figure 9 the contour lines are plotted for negative vorticity (counterclockwise rotation). By $T = 30$ the initial straight vorticity layer (velocity shear layer) has developed into a vortex train. Eight vortices appear in the early phase as predicted by the linear theory. Note that the fastest growing Fourier mode of the total kinetic energy reaches its peak amplitude around $T = 30$ (see Figure 4). At $T = 90$, four vortices appear after two neighboring vortices merged. Each vortex rotates counterclockwise, and at $T = 240$, after the second subharmonic reaches its peak amplitude (see Figure 4), two vortices are formed. At $T = 600$ a large isolated vortex appears after three consecutive vortex pairings.

Figure 10 shows contour lines of (a) pressure, (b) flow velocity vectors, and (c) current vectors at $T = 40$. The pressure is normalized by the initial uniform pressure p_0, and the velocity vectors are normalized by V_0. Figure 10a shows that eight pairs of low-pressure (rarefied) and high-pressure (compressed) regions appear along $x \sim 0$. Figure 10a shows the local minimum pressure by L and the local maximum pressure by H. The rarefied region has a much steeper pressure gradient than the compressed region. The B_z component is reduced in the low-pressure region as well, and it is enhanced in the high-pressure region, because only the fast magnetosonic mode with the change of the magnetic pressure in phase with the thermal pressure is excited by the instability in the 2-D MHD transverse configuration [*Miura and Pritchett*, 1982]. Although not clearly seen, Figure 10b shows that the initial velocity shear layer undulates and eight vortices rotating counterclockwise appear along $x \sim 0$ at $T = 40$. Note that the vortical flow appears only in the rarefied region in Figure 10a. Figure 10c shows that the eddy current flowing counterclockwise is associated with each vortex in Figure 10b. From the equation of motion the electric current $\mathbf{J}_\perp$ is calculated as

$$\mathbf{J}_\perp = \rho \frac{\mathbf{B}}{B^2} \times \frac{d\mathbf{v}}{dt} + \frac{\mathbf{B}}{B^2} \times \nabla p \quad (25)$$

Since the direction of $\mathbf{B} \times \nabla p$ is clockwise in the rarefied region and thus opposite to the direction of the observed eddy current the eddy current observed in the rarefied region in Figure 10c, associated with each flow vortex, must be the inertia current (first term of the right-hand side of (25)). In other words, the centrifugal force by the counterclockwise rotation, which is responsible for expelling the plasma outward from inside the vortex, is balanced by the sum of $\mathbf{J} \times \mathbf{B}$ force and $-\nabla p$ force directed to the center of the vortex.

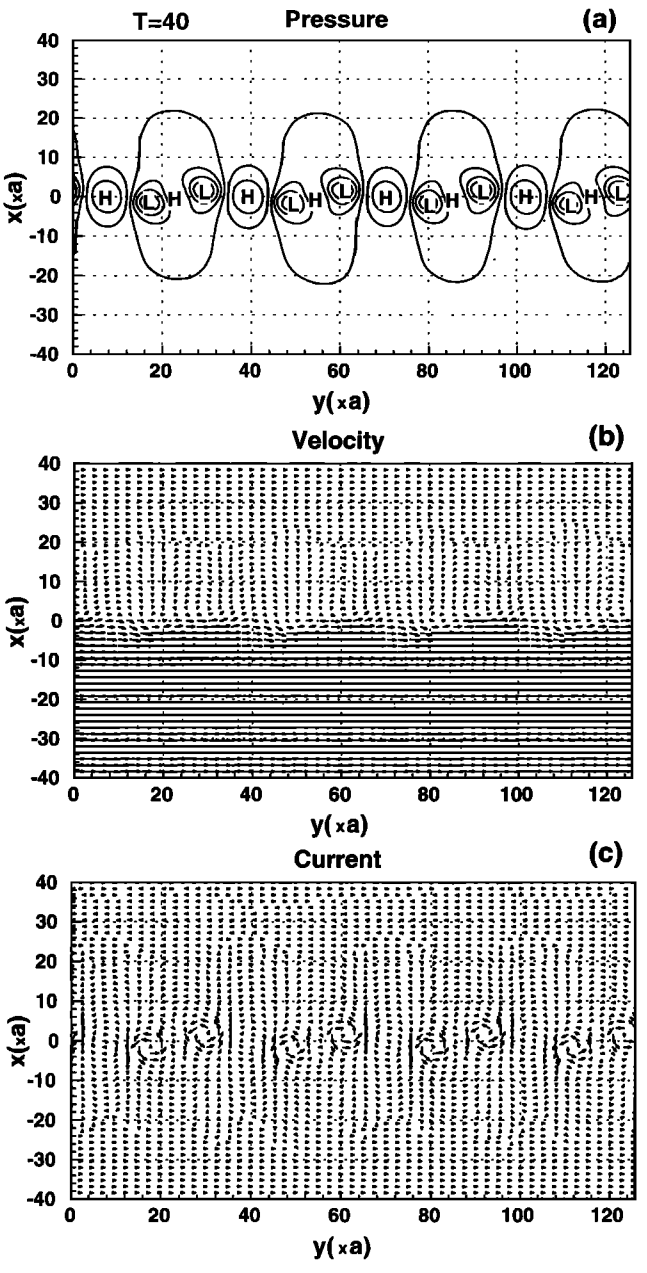

Figure 10. (a) Contour lines of pressure, (b) flow velocity vectors, and (c) current vectors at $T = 40$. H and L in Figure 10a represent the positions of maximum and minimum pressures, respectively.

Figure 11 shows the same physical quantities as are plotted in Figure 10 in the same format as Figure 10 but at $T = 90$. Figure 11a shows that four pairs of low- and high-pressure regions appear at $T = 90$ after the first vortex pairing. As is true at $T = 40$ (see Figure 10a), the pressure gradient is much stronger in the rarefied region than in the compressed region. In the rarefied region, large vortices rotating counterclockwise appear (Figure 11b). As is described in more detail later, it is seen in Figure 11b that the flow velocity is slightly enhanced or the plasma is slightly accelerated at the periphery of the vortex in $x < 0$ at $T = 90$. Figure 11c shows that four current eddies appear in the low-pressure regions in association with the large vortical flows, although the center of the current eddy is slightly shifted from the center of the flow vortex.

Figure 12 shows the same physical quantities as are plotted in Figure 10 in the same format as Figure 10 but at $T = 600$. Figure 12a shows that a pair of low- and high-pressure regions develops at $T = 600$. As is true at $T = 40$ and $T = 90$ (see Figures 10a and 11a), the pressure gradient is much stronger in the rarefied region than in the compressed region. In the rarefied region a large isolated vortex rotating counterclockwise appears (Figure 12b). Figure 12b also shows that in the compressed region between vortices the large flow momentum in the y direction in $x < 0$ is transported to $x > 0$. As is described in more detail later, it is seen in Figure 12b that the flow velocity is enhanced or the plasma is accelerated at the periph-

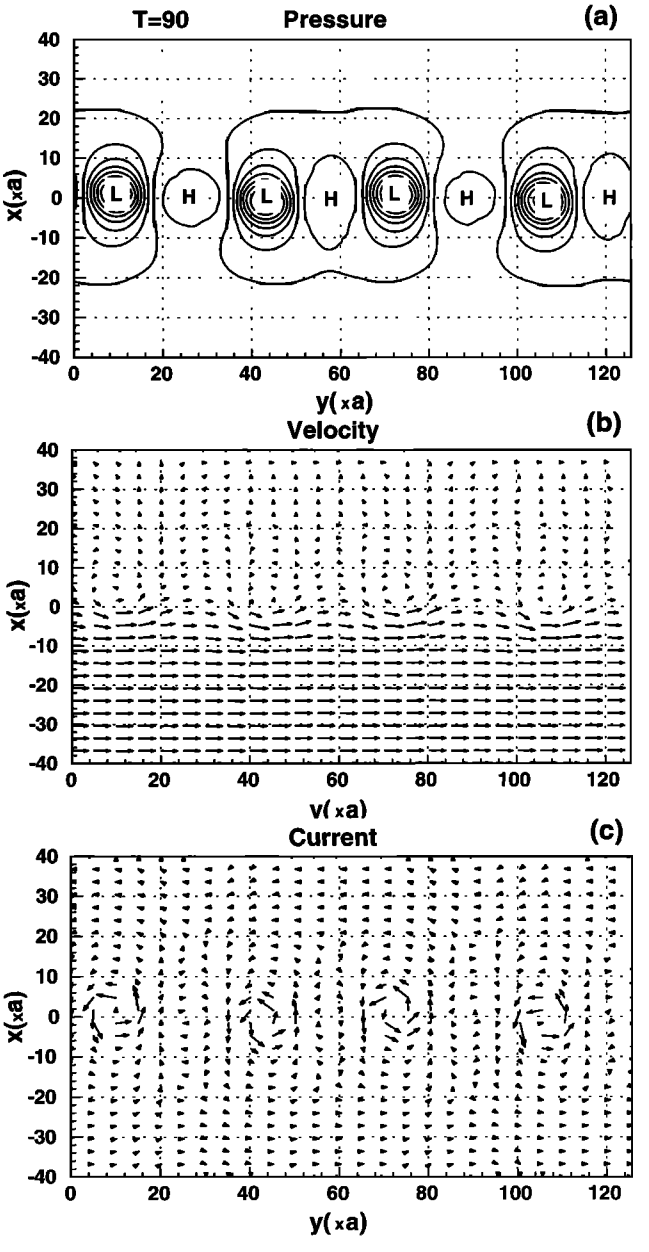

Figure 11. (a) Contour lines of pressure, (b) flow velocity vectors, and (c) current vectors at $T = 90$. H and L in Figure 11a represent the positions of maximum and minimum pressures, respectively.

ery of the vortex in $x < 0$ at $T = 600$. The flow enhancement is stronger at $T = 600$ than at $T = 90$. Figure 12c shows that a large isolated current eddy appears in the low-pressure region in association with the large isolated vortical flow. Notice as we noticed in Figure 11c that the center of the current eddy is located at $x = 0$, whereas the center of the vortex in Figure 12b is located at $x > 0$. This is because the flow velocity vector is dependent on the inertial frame of reference, but the electric current is independent of the inertial frame of reference. If we use an inertial frame of reference, wherein the background flow is antisymmetric, the center of the vortical flow will be located at $x = 0$.

Figure 13a shows contour lines of the plasma density at $T = 600$, which is normalized by the initial density ρ_0. In the 2-D MHD transverse configuration the plasma density ρ and B_z remain proportional. Therefore Figure 13a also shows contour lines of B_z normalized by the initial uniform magnetic field B_0 at $T = 600$. The low-density region located at the flow vortex has a much steeper density gradient than in the high-density region. Figure 13b shows contour lines of the plasma temperature T_p normalized by the initial uniform temperature T_0 at $T = 600$. The adiabatic cooling of the plasma occurs inside the flow vortex, and the adiabatic heating occurs between vortices. The low-temperature region located at the isolated flow vortex has a much steeper temperature gradient than the high-temperature region.

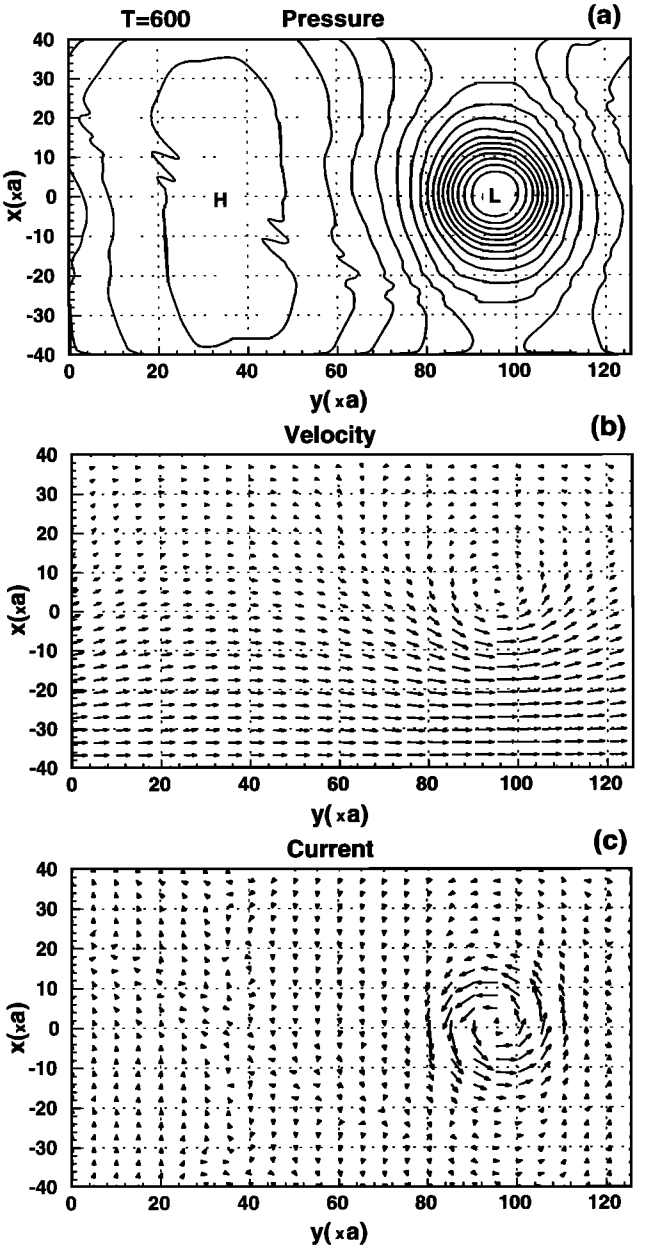

Figure 12. (a) Contour lines of pressure, (b) flow velocity vectors, and (c) current vectors at $T = 600$. H and L in Figure 12a represent the positions of maximum and minimum pressures, respectively.

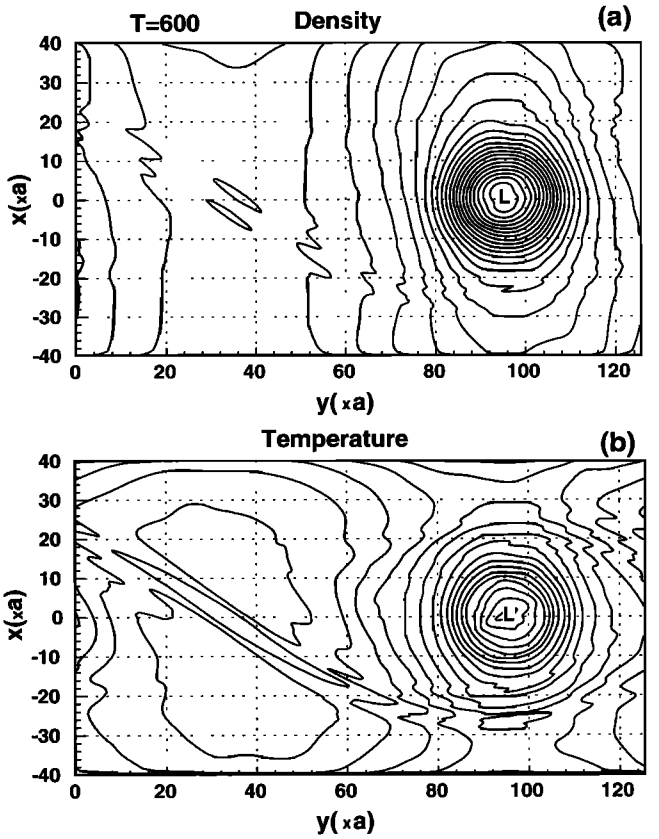

Figure 13. Contour lines of (a) density and (b) temperature at $T = 600$. L in Figures 13a and 13b represent the positions of density and temperature minimums, respectively.

Figure 14a shows profiles in the y direction of pressure p (dot-dashed curve) normalized by p_0, temperature T_p (double dot-dashed curve) normalized by T_0, density ρ (dotted curve) normalized by ρ_0, and the y component of the velocity v_y (solid curve) normalized by V_0 at $x = 0$ and at $T = 20$, when the fastest growing mode reaches a first peak (see Figure 4). The density and B_z remain proportional. Therefore the profile of the normalized B_z is the same as the profile of the normalized density ρ. As is obvious, normalized p, ρ, B_z, and T_p become <1.0, which is their original value, at their minima inside the vortex owing to a rarefaction due to the fast magnetosonic wave excited by the instability, but they become slightly larger than 1.0 at their peaks owing to a compression due to the fast magnetosonic wave. As is predicted by the linear analysis, eight pairs of local maximum and minimum of p, ρ, B_z, and T_p appear in the simulation box in the early phase at $T = 20$. The velocity component v_y at $x = 0$ undulates owing to a devel-

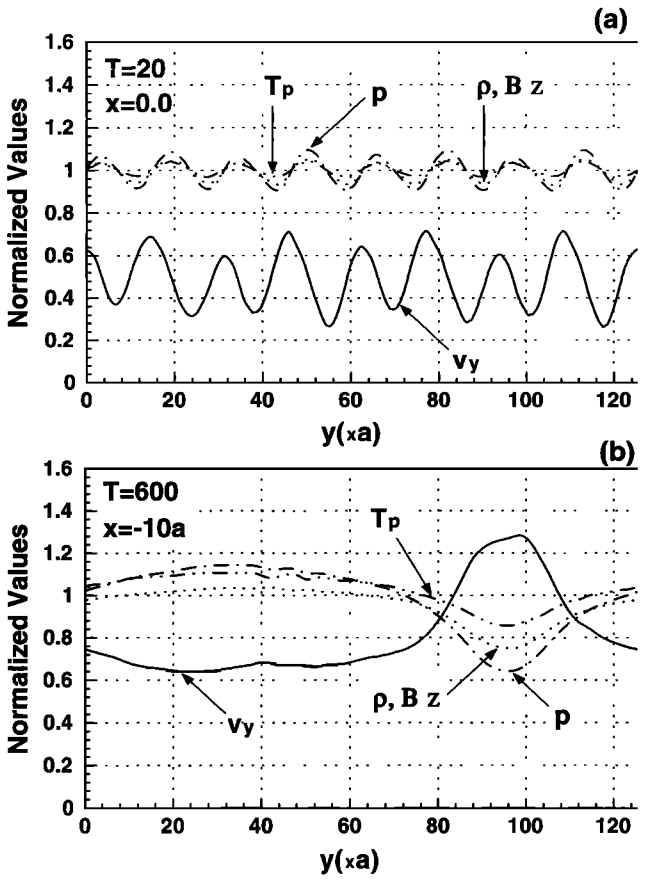

Figure 14. Profiles in the y direction of pressure p (dot-dashed curve) normalized by p_0, temperature T_p (double dot-dashed curve) normalized by T_0, density ρ (dotted curve) normalized by ρ_0, and y component of the velocity v_y (solid curve) normalized by V_0 at (a) $x = 0$ at $T = 20$ and (b) $x = -10a$ at $T = 600$.

opment of vortices, and there is about $\pi/2$ phase difference between the peaks of p, ρ, B_z, and T_p and the peak of v_y. Figure 14b shows the same profiles as in Figure 14a at $x = -10a$, which is off the vortex center, and at $T = 600$. At this time, p, ρ, B_z, and T_p have deep minima at $y \sim 95a$, and they have broad peaks near $y \sim 40a$. The normalized pressure p becomes as low as 60% of the original value (1.0) at $y \sim 95a$ because of the fast magnetosonic rarefaction. The temperature also decreases considerably within this rarefied region located at the vortex owing to an adiabatic cooling. Originally, the normalized peak velocity v_y was equal to 1.0, and therefore the plasma is strongly accelerated locally near the periphery of the vortex and the peak velocity becomes ~1.3 at $T = 600$. There is an antiphase relationship between the minima of p, ρ, B_z, and T_p and the maximum of v_y. Since the original flow speed did not exceed 1.0 this is strong evidence that the compressible K-H instability in the transverse configuration leads to a plasma flow acceleration or the flow enhancement near the periphery of the vortex owing to the fast magnetosonic rarefaction. In other words, where the perturbed vortex motion associated with the excited fast wave is in the same direction as the background flow, the flow velocity is enhanced.

Figure 15a shows the temporal evolution of the Reynolds (tangential) stress (momentum flux) $\tau = \langle \rho v_x v_y \rangle$ at $x = 0$, where the angular brackets denote the spatial average over the y direction. The Reynolds stress is normalized by $\rho_0 V_0^2$. In the present 2-D transverse configuration we obtain from the equation of motion

$$\frac{\partial}{\partial t}\langle \rho v_y \rangle = -\frac{\partial}{\partial x}\langle \rho v_x v_y \rangle \tag{26}$$

Therefore the Reynolds stress is responsible for the momentum transport [*Miura*, 1982, 1984; *Horton et al.*, 1987]. During the initial linear phase the Reynolds stress grows exponentially, and after reaching a peak it decreases toward zero. It becomes zero at $T \sim 30$, when the amplitude of the fastest growing mode reaches its peak (see Figure 4). When the vortices begin to coalesce or when the amplitude of the first subharmonic exceeds the amplitude of the fundamental mode (see Figure 4), it begins to increase again. After reaching a peak amplitude at $T \sim 50$ it decreases and becomes zero at $T \sim 55$, when the amplitude of the first subharmonic reaches its peak. Thereafter the Reynolds stress becomes negative. The Reynolds stress begins to increase when the amplitude of the second subharmonic exceeds that of the first subharmonic at $T \sim 100$ (see Figure 4). After reaching a peak at $T \sim 130$ the Reynolds stress becomes zero at $T \sim 150$. Notice that after the initial peak of the Reynolds stress at $T \sim 25$ the subsequent peaks of the Reynolds stress are about twice as large as the first peak at $T \sim 25$. Figure 15b shows the time integral of the averaged

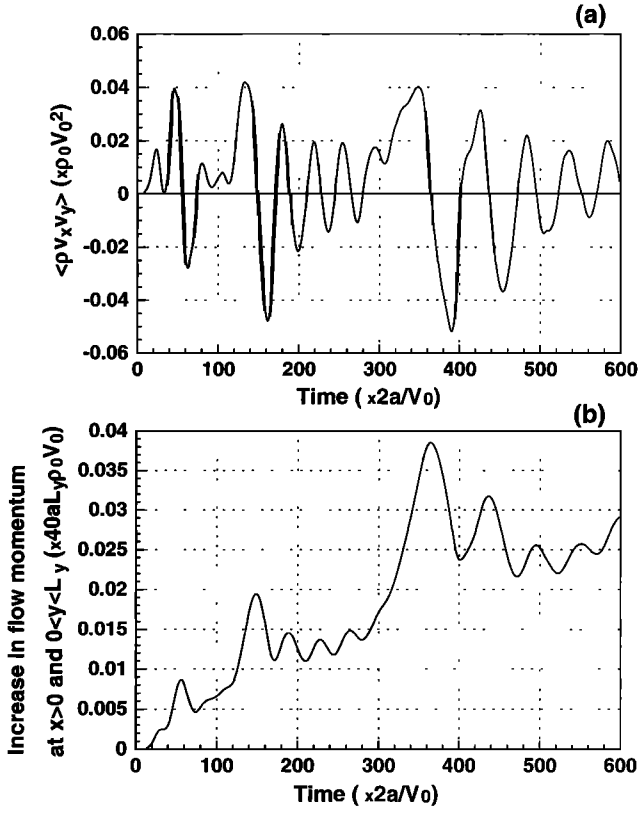

Figure 15. (a) Temporal evolution of the normalized Reynolds stress at $x = 0$ averaged over the y direction. (b) Temporal evolution of the normalized time integral of the averaged tangential stress at $x = 0$, which is equal to the total flow momentum in the positive y direction in $x > 0$.

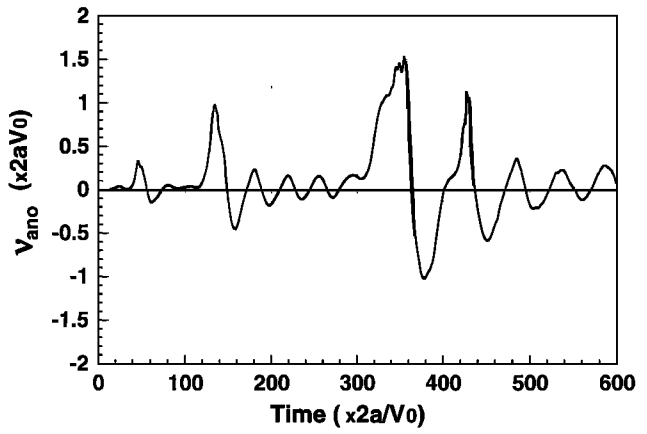

Figure 16. Temporal evolution of the normalized anomalous viscosity at $x = 0$ as a function of the normalized time.

Reynolds stress τ at $x = 0$, which is equal to the increase of the total flow momentum in the positive y direction in $x > 0$. This quantity is normalized by $40aL_y\rho_0V_0$. As long as the fastest growing mode is growing or the vortex pairing continues, the total flow momentum in the y direction in $x > 0$ increases. Therefore the net momentum transport from $x < 0$ to $x > 0$ occurs by the instability. However, after the completion of the last vortex pairing at $T \sim 340$ the Reynolds stress becomes small and the total flow momentum in $x > 0$ stays nearly at a constant value. This means that after the completion of the last vortex pairing the net momentum transport vanishes because no more vortex pairing or no more growth of a subharmonic with $k = k_{FGM}/16$ is allowed in the system owing to the finite L_y. Notice that the total flow momentum in the positive y direction in $x > 0$ has local peaks at $T \sim 30$, 60, 150, and 360 when the amplitudes of the fundamental mode, the first subharmonic, the second subharmonic, and the third subharmonic have their peak values, respectively (see Figure 4), and when the Reynolds stress becomes zero (see Figure 15a).

In order to measure quantitatively the momentum transport by the K-H instability an anomalous viscosity is defined by the following equation:

$$\nu_{ano} = -\langle \rho v_x v_y \rangle \left[\frac{d}{dx} \langle \rho v_y \rangle \right]^{-1} \tag{27}$$

This expression is analogous to the definition of the eddy viscosity [*Lamb*, 1932] in the hydrodynamics. However, the eddy viscosity is a semiempirical constant relating the Reynolds stress to the gradient of the flow momentum linearly, and it is assumed to be constant both in time and in space. Here the anomalous viscosity (27) is calculated from the simulation results, and it depends both on time and on space. Figure 16 shows the temporal evolution of the anomalous viscosity ν_{ano} at $x = 0$. It is normalized by $2aV_0$. At $T \sim 30$, ν_{ano} reaches $\sim 0.03 \cdot 2aV_0$. However, at $T \sim 50$, when the first vortex pairing begins and the first subharmonic is growing (see Figure 4), it becomes much larger than that at $T \sim 20$ and reaches $\sim 0.35 \cdot 2aV_0$. At $T \sim 140$, when the second vortex pairing begins, it reaches $\sim 2aV_0$. At $T \sim 360$, when the third subharmonic peaks, it reaches $\sim 1.5 \cdot 2aV_0$. This is ~50 times larger than that due to the growth of the linearly fastest growing mode. Note that the anomalous viscosity becomes negative when the Reynolds stress is negative. During this time, steepening of $\langle v_y \rangle$ rather than relaxation of $\langle v_y \rangle$ occurs. After the completion of the third vortex pairing by $T \sim 400$ the anomalous viscosity fluctuates around zero with a small amplitude, and there is no net momentum transport after $T \sim 400$.

Figures 17a and 17c show profiles across x of the Reynolds stress normalized by $\rho_0V_0^2$ at $T = 30$ and at $T = 360$, respectively. Figure 17b shows the flow momentum profile $\langle \rho v_y \rangle$ normalized by ρ_0V_0 (dotted curve), the flow velocity profile $\langle v_y \rangle$ normalized by V_0 (solid curve), and the x component of the electric field $\langle E_x \rangle$ normalized by V_0B_0 (dot-dashed curve), which is responsible for the $\mathbf{E} \times \mathbf{B}$ drift in the y direction, at $T = 30$. The dashed curve shows the profile $\langle v_y \rangle$ at $T = 0$, which is also equal to the initial profile of $\langle \rho v_y \rangle$. The double dot-dashed curve shows the profile of $\langle E_x \rangle$ at $T = 0$. Figure 17d shows the same quantities as those in Figure 17b at I = 360 in the same format as Figure 17b. Although the net momentum is transported from $x < 0$ to $x > 0$ by the growth of the fastest growing mode at $T = 30$ (Figure 17b) [*Miura*, 1982, 1984], much larger flow momentum is transported across $x = 0$ by the coalescence of vortices and by the growth of subharmonics at $T = 360$ (Figure 17d). Therefore a much larger relaxation of the gradient of the average of the flow momentum $\langle \rho v_y \rangle$ and $\langle v_y \rangle$ occurs at $T = 360$ (Figure 17d). Notice that at $T = 360$ (Figure 17d), there is a large penetration of $\langle E_x \rangle$ into the region of $x > 0$, which is responsible for the momentum transport from $x < 0$ to $x > 0$.

4. Discussion and Summary

The present study has established that the successive vortex pairings in the 2-D MHD transverse K-H instability are a self-organization process. In the parallel configuration, where the initial magnetic field is parallel to the initial shear flow, *Frank et al.* [1996], *Ryu et al.* [1995], and *Jones et al.* [1997] have shown by 2-D compressible MHD simulations that the initial flow relaxed to a nearly laminar flow condition in which the magnetic helicity is nearly maximized and the magnetic field is aligned with the flow. Similar simulations have also been done by *Malagoli et al.* [1996] and *Min and Lee* [1996]. In their simulations the primary source of the dissipation is a numerical resistivity. However, since their simulations were done for a system length equal to the wavelength of the linearly fastest growing mode and did not allow for the growth of the subharmonics and inverse energy cascade, that their final state, suggesting a dynamical alignment [*Dobrowolny et al.*, 1980], is the self-organized state does not seem to have been rigorously established in the parallel configuration and a further study seems to be necessary. In the present MHD transverse configuration it is possible in principle to add a small resistivity to the induction equation of the magnetic field. In such a case, there are two dissipation processes, i.e., the viscous dissipation and the resistive dissipation. It is not obvious how the selective dissipation, which now includes also the dissipation of the magnetic energy, would be changed in the presence of both viscosity and resistivity. Although the present study shows the self-organization in the 2-D MHD transverse configuration, it is not certain whether such a self-organization is possible in the 3-D MHD flow. In the 3-D hydrodynamics the enstrophy is no longer an inviscid invariant, and the vortex pairing does not occur in the 3-D hydrodynamic turbulence, unless a properly tailored 2-D seed perturbation is given initially, so that a purely 2-D disturbance can grow in the 3-D configuration [*Metcalfe et al.*, 1987]. However, the situation might be different in the 3-D

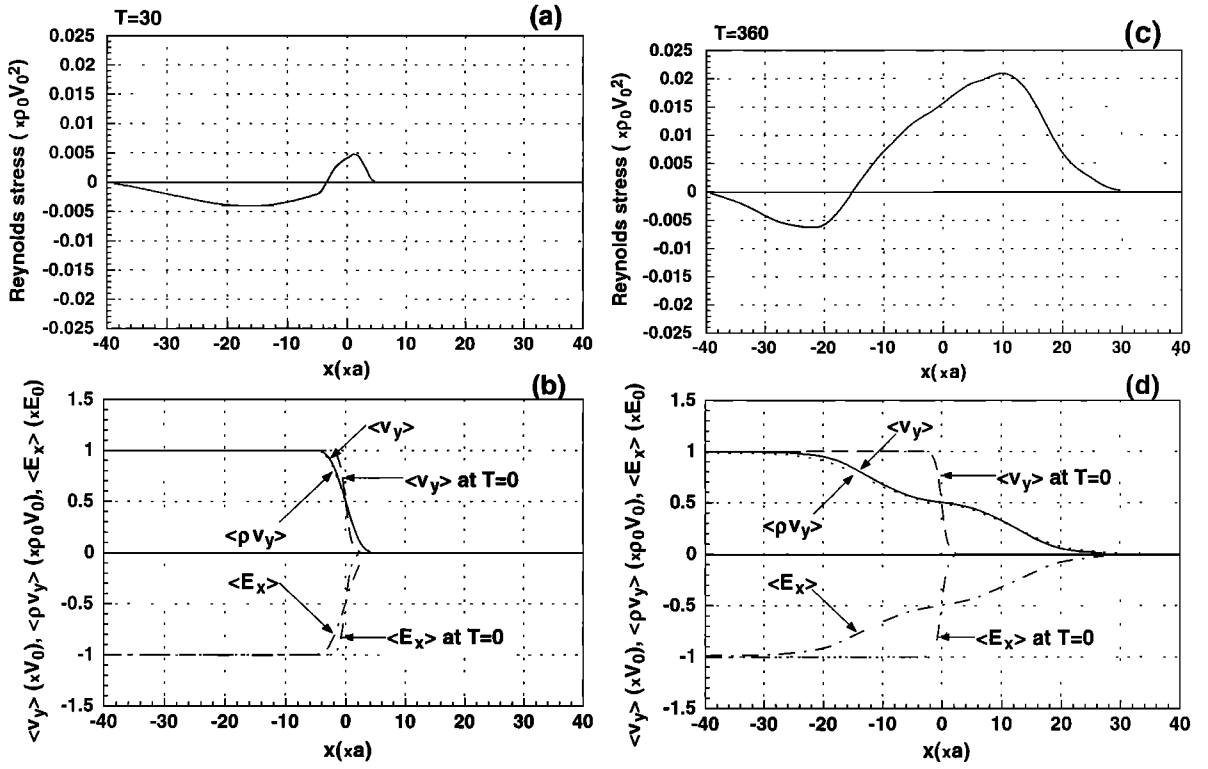

Figure 17. Profiles across x of the averaged Reynolds stress $\langle \rho v_x v_y \rangle$ at (a) $T = 30$ and (c) $T = 360$. Profiles of the x component of the averaged electric field $\langle E_x \rangle$ (dot-dashed curve), the averaged flow momentum $\langle \rho v_y \rangle$ (dotted curve), and the averaged flow velocity $\langle v_y \rangle$ (solid curve) at (b) $T = 30$ and (d) $T = 360$. The dashed profiles in Figures 17b and 17d show their initial ($T = 0$) profiles.

MHD because the force of $\mathbf{J} \times \mathbf{B}$ forces plasma to flow in a direction perpendicular to the magnetic field, and thus the 2-dimensionality of the flow in the plane perpendicular to the magnetic field may well be maintained even in the 3-D MHD when there is a strong background magnetic field.

An initial perturbation in the present simulation run, which is given by a superposition of the fundamental mode and its subharmonics, is rather artificial. A simulation run starting from a random noise has been done by *Belmont and Chanteur* [1989] for an initial configuration with a magnetic field component parallel to the flow. In their study the inverse energy cascade and the pairing of vortices have also been observed. The present simulation shows that the total kinetic energy spectrum in the final stage is well represented by a power law with the power law exponent of -3.89. This exponent is close to the value -4 obtained in the previous simulation using the Fourier spectrum method for the electrostatic K-H instability in the 2-D transverse configuration [*Miura and Sato*, 1978b]. In that simulation, physical quantities in the two-fluid equations were expanded by Fourier series in the initial flow direction, and the time evolution of each Fourier component and the Fourier spectrum of the kinetic energy were calculated locally at several x. In the present simulation the square amplitude of the Fourier component of the total kinetic energy is integrated along x, and therefore the Fourier spectra shown in Figure 5 are more or less average in the x direction. In spite of these technical differences between the present simulation and the previous one [*Miura and Sato*, 1978b], there is a good agreement of the spectral distribution of the total kinetic energy. *Lesieur et al.* [1988] also did an incompressible 2-D hydrodynamic simulation of the K-H instability starting from an initial white-noise perturbation and obtained the longitudinal kinetic energy spectrum with a power law exponent between -3 and -4, which is consistent with the present study. In the present simulation the magnetic field component B_z is also perturbed. The spectral distribution of the magnetic energy at $T = 600$ in the same wavenumber subrange as used in Figure 7 was found to be a power law form, and its power law exponent was equal to -4.58 in the present study.

Regarding the artificial viscosity added to the system, which is necessary for the selective dissipation, we should point out that in order to obtain a clear third vortex pairing after two consecutive vortex pairings the magnitude of the artificial viscosity (more precisely, the magnitude of the multiplier κ in front of the artificial viscosity term [*Miura*, 1985]) in the present run had to be increased to 8 times as large as that used in the previous simulation run with a half system length [*Miura*, 1997]. Although the relationship between the magnitude of the dissipation (viscosity in the present case) and the self-organization or the realization of the minimum energy state should be put into a more quantitative basis in the future, this fact might suggest the delicate role of a selective dissipation in the self-organization process. If a much larger artificial viscosity is used in the simulation, the K-H instability will be damped completely and will not be observed at all because it is known that the viscosity decreases the growth rate of the K-H instability [*Chandrasekhar*, 1961]. For such a large viscosity the system will reach an ultimate thermodynamic equilibrium state where the plasma is at rest and there is no structure. Therefore a finite viscosity is necessary for the self-organization, but too

large a viscosity does not lead to the self-organization. Since the viscous dissipation is larger for a higher k mode than a lower k mode it is reasonable that the enstrophy, whose spectrum has a larger power law exponent than that of the integrated kinetic energy spectrum, decays more quickly than the total kinetic energy. In the present simulation the dissipation necessary for the self-organization is provided by the artificial viscosity, which is added to prevent mesh oscillations. Although we do not ask here the nature of the viscosity in a real collisionless space plasma, previous particle and hybrid simulations [*Pritchett and Coroniti*, 1984; *Horton et al.*, 1987; *Tajima et al.*, 1991; *Thomas and Winske*, 1993; *Cai et al.*, 1993; *Fujimoto and Terasawa*, 1995; *Wilber and Winglee*, 1995] show the pairing of vortices in the 2-D transverse K-H instability. The nature of the viscosity, which must be due to ion kinetics in such collisionless plasma simulations, is unknown; however, those simulations suggest that the successive pairings of vortices or the self-organization in the K-H instability are possible in a real collisionless space plasma. In spite of the differences in the magnitude of the artificial viscosity and the length of the simulation system between the present simulation and the previous one [*Miura*, 1997] the basic characteristics obtained in the configuration space in those two simulation runs are similar with only a quantitative change. Therefore we anticipate from those two simulations with different system lengths that the basic results obtained in the simulations of the 2-D MHD transverse K-H instability regarding the vortex pairing, momentum transport, fast magnetosonic rarefaction inside the vortex, appearance of the current eddy associated with the vortex, and the flow acceleration near the periphery of the vortex remain valid for longer simulation systems.

The present simulation shows that the anomalous viscosity defined by (27) becomes negative during the evolution of the K-H instability. This means that the velocity shear is at times increased with time rather than relaxed during the evolution of the K-H instability. In addition, the plasma density and the pressure inside the vortex become smaller and smaller with the development of the vortex pairing, and thus the density gradient increases with time. These two features, which seem to contradict the second law of thermodynamics, arise because the present system with flow is not in the thermodynamic equilibrium state and indeed the system is far from equilibrium. If a much larger artificial viscosity is added to the system or a sufficiently long time elapses, it will reach an ultimate thermodynamic equilibrium state where the plasma is at rest and there is no structure. The present final self-organized state characterized by the appearance of a large isolated vortex is a metaequilibrium state [*Fine et al.*, 1995].

It should be emphasized here that a real viscosity determines only ultimate dissipation of vorticity and energy at small scales, but the transport of momentum and energy itself is governed by macroscopic vortices excited by the K-H instability. This is analogous to the ordinary hydrodynamics, wherein the kinematic viscosity determines only the ultimate dissipation of vorticity and energy at small scales but the transport of momentum itself is essentially due to turbulent eddies. Figure 16 shows that when the linearly fastest growing mode (vortex) is growing, the anomalous viscosity ν_{ano} at $x = 0$ reaches $\sim 0.03 \cdot 2aV_0$. When the third vortex pairing begins, it reaches $1.5 \cdot 2aV_0$. If a further vortex pairing and growth of a subharmonic with a longer wavelength are allowed, the anomalous viscosity will become larger than this value. This increase of the anomalous viscosity with the vortex pairings reconciles the apparent inconsistency between the simulation of *Miura* [1984] and the simulations of *Wu* [1986] and *Manuel and Samson* [1993] regarding the magnitude of the momentum transport by the instability. *Wu* [1986] suggested on the basis of simulations of the spatially evolving K-H instability that the momentum transport associated with the K-H instability is much more important than that calculated by *Miura* [1984], and *Manuel and Samson* [1995] obtained an anomalous viscosity much larger than that obtained by *Miura* [1984]. This discrepancy between simulation results of *Miura* [1984] and those of *Wu* [1986] and *Manuel and Samson* [1993] regarding the magnitude of the anomalous momentum transport by the instability is ascribable to the fact that in the simulation of *Miura* [1984] the vortex pairing was not allowed and therefore the anomalous viscosity obtained by his study is small because it is due only to the growth of the fastest growing vortex, while the simulations of spatial development of the K-H instability by *Wu* [1986] and *Manuel and Samson* [1993] allowed the vortex pairings and thus yielded a much larger momentum transport or the anomalous viscosity.

The present self-organization mechanism in the 2-D K-H instability may be applicable to a wide variety of phenomena observed in space, which are due to sheared flow. For example, it has been suggested [e.g., *Prigogine*, 1980] that an emergence of a large vortex out of small vortices excited by the K-H instability in the wind shear may be responsible for the appearance of the great red spot in Jupiter's atmosphere. In practical problems such as the K-H instability at the magnetopause and at the bow shock [*Leboeuf et al.*, 1981; *Murawski and Steinolfson*, 1996] the spatial growth of the K-H instability [*Brown and Roshko*, 1974; *Wu*, 1986; *Manuel and Samson*, 1993; *Thomas and Winske*, 1993; *Wei and Lee*, 1993] is more common than the temporal growth as treated here. Since those simulations of the spatial growth of the K-H instability using the nonperiodic boundary condition [*Wu*, 1986; *Manuel and Samson*, 1993; *Thomas and Winske*, 1993; *Wei and Lee*, 1993] show vortex pairings in the downstream the appearance of the successive vortex pairings or the self-organization in the 2-D K-H instability is rather insensitive to the choice of the boundary condition in the initial flow direction. In such spatial growth of the K-H instability the large momentum transport by the vortex pairing in the K-H instability is expected in the downstream region of the sheared plasma flow. It follows that a very large momentum transport is expected across the distant tail magnetopause because the vortices undergo several vortex pairings before they reach the tail magnetopause. Since the temporal evolution of the K-H instability in the present study can be transformed to a spatial growth along the velocity shear layer [*Miura*, 1997] it is suggested that small-scale vortices created by the instability near the subsolar magnetopause evolve into global-scale vortices in the distant magnetospheric tail. The simple estimate based on the simulation results suggests that the four or five vortex pairings occur before the vortices reach the distant tail magnetopause. Therefore the wavelength of the vortex becomes $2^4 \sim 2^5 = 16 \sim 32$ times as long as the wavelength of the linearly fastest growing vortex. If the fastest growing vortex has a wavelength of $1.0Re$ near the dayside magnetopause, its wavelength becomes $\sim 32Re$ in the distant tail magnetopause, which is comparable to the size of the magnetosphere. Therefore the basic characteristics of the K-H instability such as the momentum transport appears on a global scale at the distant tail magnetopause. The relevance of the self-organization, which is manifest on the nonlinear develop-

ment of the K-H instability, to observed phenomena in space, such as the magnetopause K-H instability, will be discussed more quantitatively elsewhere. In particular, this self-organization hypothesis of the magnetopause K-H instability will be tested against reported observations of the magnetopause oscillation in a later publication. Notice that the present simulation, wherein the initial magnetic field is assumed to be everywhere perpendicular to the flow is considered to be a case for interplanetary magnetic field (IMF) due north, when the magnetopause is most susceptible to the K-H instability [*Miura*, 1995a, b]. Notice also in Figures 10–12 that the vortices or vortical flows are located inside the velocity shear region, i.e., in the magnetospheric region, while the center of the vorticity in Figure 9 and the centers of current eddies in Figures 10–12 are located at the center of the velocity shear region, i.e., at the magnetopause. This is because the vorticity, the magnetic field, and the electric current are independent of an observing inertial frame, i.e., invariant for the Galilean transformation, whereas the flow velocity, the vortical flow, and hence the location of the vortex are dependent on an observing inertial frame (Galilean variant). Although the vortical flows are located in the magnetosphere inside the velocity shear layer when the rest frame of the magnetosphere is used as an inertial frame as in the present simulation [see also *Miura*, 1992, 1995b], the centers of the vortical flows are located at the center of the velocity shear layer, i.e., at the magnetopause, when a simulation is done in an inertial frame in which the flow is antisymmetric and the vortices are stationary [*Miura*, 1984].

In summary, the present study has established that the successive vortex pairings in the nonlinear evolution of the two-dimensional MHD transverse K-H instability are an emergence of the self-organization process resulting from the interplay of the nonlinearity and the dissipation (viscosity in the present case), which causes the irreversibility. Although the K-H instability is essentially an inviscid phenomenon (viscosity plays only a stabilizing role and not a destabilizing role), the self-organization in its nonlinear stage, i.e., the successive vortex pairings in the nonlinear stage, is due to viscosity, which leads to selective dissipation. The self-organization leads to an emergence of a large-scale vortex out of a train of small-scale vortices in the early stage by the inverse cascade. The dependence of the self-organization on the magnitude of the viscosity (Reynolds number) and the compressibility (Mach number) should be investigated in a more quantitative manner in the future. The effect of using a different initial seed perturbation and the effect of the initial magnetic field parallel to the flow on the self-organization process should also be investigated in order to understand completely the self-organization process in the K-H instability in more realistic configurations in space plasmas.

Acknowledgments. This work has been supported by Grants-in-Aid for Scientific Research 09640529, provided by the Ministry of Education, Science, Sports, and Culture, and, in part, by the Radio Atmospheric Sciences Center of Kyoto University and the Institute of Space and Astronautical Science of the Ministry of Education, Science, Sports, and Culture as a joint research project. This work was also supported, in part, by the Interministry Fundamental Research Program of the Science and Technology Agency at the Communications Research Laboratory of the Ministry of Posts and Telecommunications. The computation for this work was performed at the computer center of the University of Tokyo.

The Editor thanks D. Winske, V. H. Thomas, and another referee for their assistance in evaluating this paper.

References

Batchelor, G. K., *The Theory of Homogeneous Turbulence*, p. 187, Cambridge Univ. Press, New York, 1953.

Belmont, G., and G. Chanteur, Advances in magnetopause Kelvin-Helmholtz instability studies, *Phys. Scr.*, *40*, 124, 1989.

Biskamp, D., MHD turbulence, in *Nonlinear Magnetohydrodynamics*, chap. 7, p. 175, Cambridge Univ. Press, New York, 1993.

Bretherton, F. P., and D. B. Haidvogel, Two-dimensional turbulence above topography, *J. Fluid Mech.*, *78*, 129, 1976.

Browand, F. K., and P. D. Weidman, Large scales in the developing mixing layer, *J. Fluid Mech.*, *76*, 127, 1976.

Brown, G. L., and A. Roshko, On density effects and large structure in turbulent mixing layer, *J. Fluid Mech.*, *64*, 775, 1974.

Cai, D., L. R. O. Storey, and T. Itoh, Particle simulation of the kinetic Kelvin-Helmholtz instability in a magnetoplasma, *Phys. Plasmas*, *5*, 3507, 1993.

Chandrasekhar, S., The stability of superposed fluids: The Kelvin-Helmholtz instability, in *Hydrodynamic and Hydromagnetic Stability*, chap. XI, p. 481, Oxford Univ. Press, New York, 1961.

Chen, S.-H., M. G. Kivelson, J. T. Gosling, R. J. Walker, and A. J. Lazarus, Anomalous aspects of magnetosheath flow and shape and oscillation of the magnetopause during an interval of strongly northward interplanetary magnetic field, *J. Geophys. Res.*, *98*, 5727, 1993.

Dobrowolny, M., A. Mangeney, and P. Veltri, Fully developed anisotropic hydromagnetic turbulence in interplanetary space, *Phys. Rev. Lett.*, *45*, 144, 1980.

Dungey, J. W., in *Proceedings of the Conference of the Ionosphere*, p. 225, Phys. Soc., London, 1955.

Fine, K. S., A. C. Cass, W. G. Flynn, and C. F. Driscoll, Relaxation of 2D turbulence to vortex crystals, *Phys. Rev. Lett.*, *75*, 3277, 1995.

Frank, A., T. W. Jones, D. Ryu, and J. B. Gaalaas, The MHD Kelvin-Helmholtz instability: A two-dimensional numerical study, *Astrophys. J.*, *460*, 777, 1996.

Fujimoto, M., and T. Terasawa, Anomalous ion mixing within an MHD scale Kelvin-Helmholtz vortex, 2, Effects of inhomogeneity, *J. Geophys. Res.*, *100*, 12,025, 1995.

Gell-Mann, M., *The Quark and the Jaguar, Adventures in the Simple and the Complex*, W. H. Freeman, New York, 1994.

Hasegawa, A., Self-organization processes in continuous media, *Adv. Phys.*, *34*, 1, 1985.

Ho, C.-M., and L.-S. Huang, Subharmonics and vortex merging in mixing layers, *J. Fluid Mech.*, *119*, 443, 1982.

Horiuchi, R., and T. Sato, Self-organization and energy relaxation in a three-dimensional magnetohydrodynamic plasma, *Phys. Fluids*, *29*, 1161, 1986.

Horton, W., T. Tajima, and T. Kamimura, Kelvin-Helmholtz instability and vortices in magnetized plasma, *Phys. Fluids*, *30*, 3485, 1987.

Jones, T. W., J. B. Gaalaas, D. Ryu, and A. Frank, The MHD Kelvin-Helmholtz instability, II, The roles of weak and oblique fields in planar flows, *Astrophys. J.*, *482*, 230, 1997.

Kivelson, M. G., and S.-H. Chen, The magnetopause: Surface waves and instabilities and their possible dynamical consequences, in *Physics of the Magnetopause*, *Geophys. Monogr. Ser.*, vol. 90, edited by P. Song, B. U. Ö. Sonnerup, and M. F. Thomsen, p. 257, AGU, Washington, D. C., 1995.

Kraichnan, R. H., Inertial ranges in two-dimensional turbulence, *Phys. Fluids*, *10*, 1417, 1967.

Kraichnan, R. H., and D. Montgomery, Two-dimensional turbulence, *Rep. Prog. Phys.*, *43*, 547, 1980.

Lamb, H., *Hydrodynamics*, 6th ed., p. 668, Cambridge Univ. Press, New York, 1932.

Landau, L. D., and E. M. Lifshitz, *Fluid Mechanics*, Pergamon, Tarrytown, N. Y., 1959.

Lapidus, A., A detached shock calculation by second-order finite differences, *J. Comput. Phys.*, *2*, 154, 1967.

Leboeuf, J. N., T. Tajima, C. F. Kennel, and J. M. Dawson, Global simulations of the three-dimensional magnetosphere, *Geophys. Res. Lett.*, *8*, 257, 1981.

Lele, S., Direct numerical simulation of compressible free shear flows, paper presented at 27th Aerospace Science Meeting, Am. Inst. of Aeronaut. and Astronaut., Reno, Nev., Jan. 1989.

Lepping, R. P., and L. F. Burlaga, Geomagnetopause surface fluctuations observed by Voyager 1, *J. Geophys. Res.*, *84*, 7099, 1979.

Lesieur, M., C. Staquet, P. Le Roy, and P. Conte, The mixing layer and its coherence examined from the point of view of two-dimensional turbulence, *J. Fluid Mech.*, *192*, 511, 1988.

Lilly, D. K., Numerical simulation of two-dimensional turbulence, *Phys. Fluids.*, *12*, 240, 1969.

Malagoli, A., G. Bodo, and R. Rosner, On the nonlinear evolution of magnetohydrodynamic Kelvin-Helmholtz instabilities, *Astrophys. J.*, *456*, 708, 1996.

Manuel, J. R., and J. C. Samson, The spatial development of the lowlatitude boundary layer, *J. Geophys. Res.*, *98*, 17367, 1993.

Matthaeus, W. H., and D. Montgomery, Selective decay hypothesis at high mechanical and magnetic Reynolds numbers, *Ann. N. Y. Acad. Sci.*, *357*, 203, 1980.

McWilliams, J. C., The emergence of isolated coherent vortices in turbulent flow, *J. Fluid Mech.*, *146*, 21, 1984.

Metcalfe, R. W., S. A. Orszag, M. E. Brachet, S. Menon, and J. J. Riley, Secondary instability of a temporally growing mixing layer, *J. Fluid Mech.*, *184*, 207, 1987.

Min, K. W., and D. Y. Lee, Simulation of Kelvin-Helmholtz instability in resistive plasma, *Geophys. Res. Lett.*, *23*, 3667, 1996.

Miura, A., Nonlinear evolution of the magnetohydrodynamic Kelvin-Helmholtz instability, *Phys. Rev. Lett.*, *49*, 779, 1982.

Miura, A., Anomalous transport by magnetohydrodynamic Kelvin-Helmholtz instabilities in the solar wind-magnetosphere interaction, *J. Geophys. Res.*, *89*, 801, 1984.

Miura, A., Anomalous transport by Kelvin-Helmholtz instabilities, in *Computer Simulation of Space Plasmas*, edited by H. Matsumoto and T. Sato, p. 203, D. Reidel, Norwell, Mass., 1985.

Miura, A., Kelvin-Helmholtz instability at the magnetospheric boundary: Dependence on the magnetosheath sonic Mach number, *J. Geophys. Res.*, *97*, 10,655, 1992.

Miura, A., Dependence of the magnetopause Kelvin-Helmholtz instability on the orientation of the magnetosheath magnetic field, *Geophys. Res. Lett.*, *22*, 2993, 1995a.

Miura, A., Kelvin-Helmholtz instability at the magnetopause: Computer simulations, in *Physics of the Magnetopause, Geophys. Monogr. Ser.*, vol. 90, edited by P. Song, B. U. Ö. Sonnerup, and M. F. Thomsen, p. 285, AGU, Washington, D. C., 1995b.

Miura, A., Compressible magnetohydrodynamic Kelvin-Helmholtz instability with vortex pairing in the two-dimensional transverse configuration, *Phys. Plasmas*, *4*, 2871, 1997.

Miura, A., and P. L. Pritchett, Nonlocal stability analysis of the MHD Kelvin-Helmholtz instability in a compressible plasma, *J. Geophys. Res.*, *87*, 7431, 1982.

Miura, A., and T. Sato, Theory of vortex nutation and amplitude oscillation in an inviscid shear instability, *J. Fluid Mech.*, *86*, 33, 1978a.

Miura, A., and T. Sato, Shear instability: Auroral arc deformation and anomalous momentum transport, *J. Geophys. Res.*, *83*, 2109, 1978b.

Montgomery, D. C., Introduction to the theory of fluid and magnetofluid turbulence, in *Nagoya Lectures in Plasma Physics and Controlled Fusion*, edited by Y. H. Ichikawa and T. Kamimura, p. 207, Tokai Univ. Press, Tokyo, 1989.

Montgomery, D., L. Turner, and G. Vahala, Three-dimensional magnetohydrodynamic turbulence in cylindrical geometry, *Phys. Fluids*, *21*, 757, 1978.

Murawski, K., and R. S. Steinolfson, Numerical simulations of mass loading in the solar wind interaction with Venus, *J. Geophys. Res.*, *101*, 2547, 1996.

Nicolis, G., and I. Prigogine, *Self-Organization in Nonequilibrium Systems: From Dissipative Structures to Order Through Fluctuations*, John Wiley, New York, 1977.

Onsager, L., *Nuovo Cimento Suppl.*, *6*, 279, 1949.

Papamoshou, D., and A. Roshko, The compressible turbulent shear layer: An experimental study, *J. Fluid Mech.*, *197*, 453, 1988.

Prigogine, I., *From Being to Becoming: Time and Complexity in the Physical Sciences*, W. H. Freeman, New York, 1980.

Prigogine, I., *The end of Certainty: Time, Chaos, and the New Laws of Nature*, Free Press, New York, 1997.

Pritchett, P. L., and F. V. Coroniti, The collisionless macroscopic Kelvin-Helmholtz instability, 1, Transverse electrostatic mode, *J. Geophys. Res.*, *89*, 168, 1984.

Pu, Z. Y., and M. G. Kivelson, Kelvin-Helmholtz instability at the magnetopause: Solution for compressible plasmas, *J. Geophys. Res.*, *88*, 841, 1983.

Rankin, R., P. Frycz, J. C. Samson, and V. T. Tikhonchuk, Shear-flow vortices in magnetospheric plasmas, *Phys. Plasmas*, *4*, 829, 1997.

Rhines, P., Waves and turbulence on a beta-plane, *J. Fluid Mech.*, *69*, 417, 1975.

Richtmyer, R. D., and K. W. Morton, *Difference Methods for Initial Value Problems*, 2nd ed., Wiley-Interscience, New York, 1967.

Riyopoulos, S., A. Bondeson, and D. Montgomery, Relaxation toward states of minimum energy in a compact torus, *Phys. Fluids*, *25*, 107, 1982.

Ryu, D., T. W. Jones, and A. Frank, Numerical magnetohydrodynamics in astrophysics: Algorithm and tests for multidimensional flow, *Astrophys. J.*, *452*, 785, 1995.

Sato, T., and the Complexity Simulation Group, Complexity in plasma: From self-organization to geodynamo, *Phys. Plasmas*, *3*, 2135, 1996.

Schardt, A. W., K. W. Behannon, R. P. Lepping, J. F. Carbary, A. Eviatar, and G. L. Siscoe, The outer magnetosphere, in *Saturn*, edited by T. Gehrels and M. S. Matthews, p. 416, Univ. of Ariz. Press, Tucson, 1984.

Seon, J., L. A. Frank, A. J. Lazarus, and R. P. Lepping, Surface waves on the tailward flanks of the Earth's magnetopause, *J. Geophys. Res.*, *100*, 11,907, 1995.

Southwood, D. J., The hydromagnetic stability of the magnetospheric boundary, *Planet. Space Sci.*, *16*, 587, 1968.

Tajima, T., W. H. Horton, P. J. Morrison, J. Schutkeher, T. Kamimura, K. Mima, and Y. Abe, Instabilities and vortex dynamics in shear flow of magnetized plasmas, *Phys. Plasmas*, *3*, 938, 1991.

Taylor, J. B., Relaxation of toroidal plasma and generation of reverse magnetic fields, *Phys. Rev. Lett.*, *33*, 1139, 1974.

Thomas, V. A., and D. Winske, Kinetic simulations of the Kelvin-Helmholtz instability at the magnetopause, *J. Geophys. Res.*, *98*, 11,425, 1993.

Walker, A. D. M., The Kelvin-Helmholtz instability in the low-latitude boundary layer, *Planet. Space Sci.*, *29*, 1119, 1981.

Wei, C. Q., and L. C. Lee, Coupling of magnetopause-boundary layer to the polar ionosphere, *J. Geophys. Res.*, *98*, 5707, 1993.

Wiener, N., *Cybernetics: Or Control and Communication in the Animal and the Machine*, 2nd ed., MIT Press, Cambridge, Mass., 1961.

Wilber, M., and R. M. Winglee, Dawn-dusk asymmetries in the low-latitude boundary layer arising from the Kelvin-Helmholtz instability: A particle simulation, *J. Geophys. Res.*, *100*, 1883, 1995.

Winant, C. D., and F. K. Browand, Vortex pairing: The mechanism of turbulent mixing-layer growth at moderate Reynolds number, *J. Fluid Mech.*, *63*, 237, 1974.

Wu, C. C., Kelvin-Helmholtz instability at the magnetopause boundary, *J. Geophys. Res.*, *91*, 3042, 1986.

A. Miura, Department of Earth and Planetary Physics, University of Tokyo, Bunkyo-ku, Tokyo 113-0033, Japan. (miura@sunep1.geoph.s.u-tokyo.ac.jp)

(Received May 20, 1998; revised July 30, 1998;
accepted July 30, 1998.)